

BAYESIAN ESTIMATES OF ASTRONOMICAL TIME DELAYS BETWEEN GRAVITATIONALLY LENSED STOCHASTIC LIGHT CURVES

BY HYUNGSUK TAK^{*}, KAISEY MANDEL[†], DAVID A. VAN DYK[‡], VINAY L. KASHYAP[†], XIAO-LI MENG^{*}, AND ANETA SIEMIGINOWSKA[†]

Harvard University, Harvard-Smithsonian Center for Astrophysics, and Imperial College London

The gravitational field of a galaxy can act as a lens and deflect the light emitted by a more distant object such as a quasar. If the galaxy is a strong gravitational lens, it can produce multiple images of the same quasar in the sky. Since the light in each gravitationally lensed image traverses a different path length from the quasar to the Earth, fluctuations in the source brightness are observed in the several images at different times. The time delay between these fluctuations can be used to constrain cosmological parameters and can be inferred from the time series of brightness data or light curves of each image. To estimate the time delay, we construct a model based on a state-space representation for irregularly observed time series generated by a latent continuous-time Ornstein-Uhlenbeck process. We account for microlensing, an additional source of independent long-term extrinsic variability, via a polynomial regression. Our Bayesian strategy adopts a Metropolis-Hastings within Gibbs sampler. We improve the sampler by using an ancillarity-sufficiency interweaving strategy and adaptive Markov chain Monte Carlo. We introduce a profile likelihood of the time delay as an approximation of its marginal posterior distribution. The Bayesian and profile likelihood approaches complement each other, producing almost identical results; the Bayesian method is more principled but the profile likelihood is simpler to implement. We demonstrate our estimation strategy using simulated data of doubly- and quadruply-lensed quasars, and observed data from quasars *Q0957+561* and *J1029+2623*.

1. Introduction. Quasars are highly luminous astronomical sources in the distant Universe. The path that light takes from a quasar to Earth can be altered by the gravitational field of a massive intervening galaxy which thus

^{*}Department of Statistics, Harvard University, 1 Oxford St., Cambridge, MA, USA

[†]Harvard-Smithsonian Center for Astrophysics, 60 Garden St., Cambridge, MA, USA

[‡]Statistics Section, Department of Mathematics, Imperial College London, London SW7 2AZ UK

Keywords and phrases: Gravitational lensing, Microlensing, Ornstein-Uhlenbeck process, Gibbs sampler, Profile likelihood, Ancillarity-sufficiency interweaving strategy, Adaptive MCMC, Q0957+561, J1029+2623, LSST

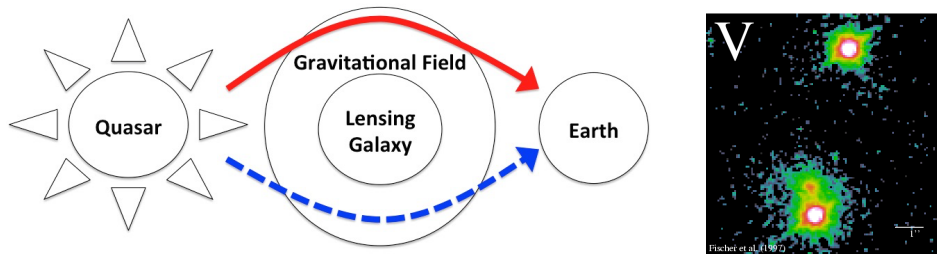


FIG 1. The gravitational field of an intervening galaxy acts as a lens deflecting two light rays of a quasar image towards the Earth as shown in the left panel. The arrival times can differ owing to the different lengths of pathways and different gravitational potentials they pass through. An optical V-band image of the doubly-lensed quasar Q0957+561 obtained with the Canada France Hawaii telescope (Fischer et al., 1997; Munoz et al., 1998) (<https://www.cfa.harvard.edu/castles>) appears in the right panel. The two bright sources at the top and bottom are the lensed images of the quasar, and the small red point towards the top-left of the lower quasar image is the lensing galaxy.

acts as a lens, bending the trajectory of the emitted light; see the first panel of Figure 1. If the gravitational field of the galaxy is a strong gravitational lens, multiple images of the quasar can appear in slightly different locations in the sky, from the perspective of an observer on Earth, an effect known as strong gravitational lensing (Schneider, Ehlers and Falco, 1992; Schneider, Wambsganss and Kochanek, 2006). In this case, there are typically two or four replicate images, referred to as doubly- or quadruply-lensed quasars.

The light rays forming each of these gravitationally lensed quasar images take different routes from the quasar to Earth. Since both the lengths of the pathways and the gravitational potentials they traverse differ, the resulting multiple images are subject to differing lensing magnifications and their light rays arrive at the observer at different times. Because of this, any fluctuations in the source brightness are observed in each image at different times. From a statistical perspective, we can construct a time series of the brightness of each image, known as a *light curve*. Features in these light curves appear to be shifted in time and these shifts are called *time delays*.

Obtaining accurate time delay estimates is important in cosmology because they can be used to address fundamental questions regarding the origin and evolution of the Universe. For instance, Refsdal (1964) suggested using time delay estimates to constrain the Hubble constant H_o , the current expansion rate of the Universe; given a model for the mass distribution and gravitational potential of the lensing galaxy, the time delay between multiple images of the lensed quasar is inversely proportional to H_o (Blandford and Narayan, 1992; Suyu et al., 2013). Also, Linder (2011) showed that

an accurate time delay estimate could substantially constrain cosmological parameters in the equation of state of dark energy characterizing the accelerated expansion of the Universe.

The upcoming large-scale astronomical survey conducted with the Large Synoptic Survey Telescope (LSST, [LSST Science Collaboration, 2009](#)), will monitor thousands of gravitationally lensed quasars beginning in 2022. The LSST is the top-ranked ground-based telescope project in the 2010 Astrophysics Decadal Survey, and will produce extensive high-cadence time series observations of the full sky for ten years. In preparation for the *Big Data* era of the LSST, [Dobler et al. \(2015\)](#) organized a blind competition called the Time Delay Challenge (TDC) which ran from October 2013 to July 2014 with the aim of improving time delay estimation methods for application to realistic observational data sets. The TDC organizers prepared thousands of simulated data sets mimicking real quasar data. We are among 13 teams who took part in the TDC, each of which analyzed the simulated data using their own methods to estimate the blinded time delays¹.

1.1. Data and challenges. We plot a pair of simulated light curves from a doubly-lensed quasar in Figure 2; the light curves are labeled as *A* and *B*. Each observation time is denoted by vertical dashed lines, at which the observer measures the brightness of each gravitationally lensed quasar image. In a real data analysis, these images would correspond to the two bright sources in the second panel of Figure 1. The brightness is reported on the magnitude scale, an astronomical logarithmic measure of brightness, in which smaller numbers correspond to brighter objects. The magnitudes in Figure 2 are presented up to an overall additive calibration constant. Since the time delay is estimated via relative comparison between fluctuations in the two light curves, it is insensitive to this overall additive constant.

For a doubly-lensed quasar, there are four variables recorded on an irregularly spaced sequence of observation times $\mathbf{t} = (t_1, t_2, \dots, t_n)^\top$; the observed magnitudes $\mathbf{x}(\mathbf{t}) = (x(t_1), x(t_2), \dots, x(t_n))^\top$ for light curve *A* and $\mathbf{y}(\mathbf{t}) = (y(t_1), y(t_2), \dots, y(t_n))^\top$ for light curve *B* as well as the standard deviations of the measurement errors of the two light curves $\boldsymbol{\delta}(\mathbf{t}) = (\delta(t_1), \delta(t_2), \dots, \delta(t_n))^\top$ and $\boldsymbol{\eta}(\mathbf{t}) = (\eta(t_1), \eta(t_2), \dots, \eta(t_n))^\top$, respectively. In Figure 2, $\mathbf{x}(\mathbf{t})$ and $\mathbf{y}(\mathbf{t})$ are represented by red squares and blue circles, and their measurement standard errors by the half lengths of vertical lines

¹In the last stage of the TDC (called *rung4* in the TDC), an earlier version of our method achieved the smallest average coefficient of variation (*precision*), the TDC target for the average error level (*accuracy*) within one standard deviation, and acceptable average squared standardized residual (χ^2) after analyzing the second highest number of data sets (*f*). See [Liao et al. \(2015\)](#) for detailed result of the TDC.

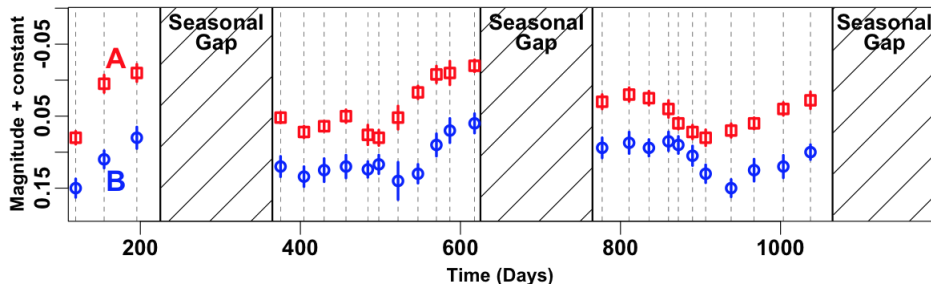


FIG 2. The red squares and blue circles indicate the observed magnitudes of the two simulated images at each observation time. The half lengths of vertical lines represent the standard deviations of the measurement errors. The convention in astrophysics is to plot the magnitude inversely so that smaller magnitudes (brighter object) appear on the top and larger ones (fainter object) on the bottom. The quasar magnitudes are vertically offset by an overall calibration constant, the value of which is unimportant for time delay estimation.

around the magnitudes. Similarly, for a quadruply-lensed quasar, there are four light curves, each with their own measurement errors.

Since a quasar exhibits fluctuations in its brightness, it is possible to estimate time delays between different copies of those fluctuations. In Figure 2, for example, the bottom of the V-shaped valley of light curve A at around 900 days precedes that of light curve B by around 50 days. Other features in the light curves exhibit a similar time delay of about 50 days.

However, a number of aspects of the light curves in Figure 2 make accurate time delay estimation statistically challenging. First, irregular observation times are inevitable because poor weather sometimes prevents observations. Second, the motion of the Earth around the Sun causes seasonal gaps because part of the sky is not visible at night during certain months. Third, since the light of each gravitationally lensed image traverses different paths through the gravitational potential, they are subject to differing degrees of lensing magnification. Thus, the light curves often exhibit different average magnitudes. Finally, observed magnitudes are measured with error, leading to relatively larger measurement errors for fainter images.

Moreover, some quasar images exhibit additional independent extrinsic variability, an effect called *microlensing*. This occurs when gravitational lensing by stars moving inside the lensing galaxy independently introduces brightness magnification variations into each path of light, in addition to the overall magnifications caused by strong lensing of the galaxy (Chang and Refsdal, 1979; Tewes, Courbin and Meylan, 2012). If the timescale of the microlensing variability is much larger than that of the intrinsic quasar

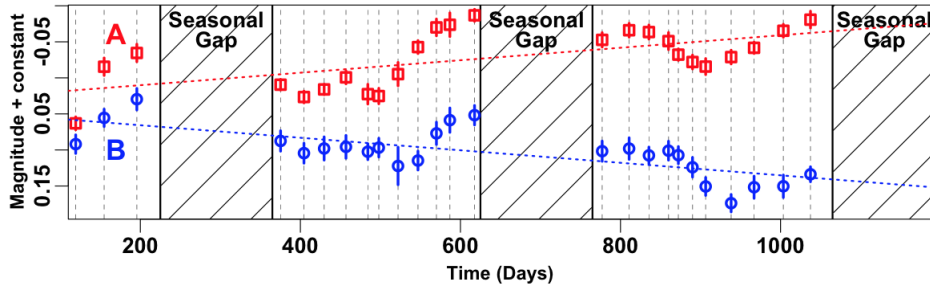


FIG 3. The light curves of two lensed images can have different long-term trends caused by microlensing due to stars moving within the lensing galaxy. This effect independently introduces a long-term magnification trend in each image. Here, we simulate the effect of two different long-term linear microlensing trends on the light curves in Figure 2. The dotted lines depict the linear microlensing trend for each image.

variability, the individual light curves may exhibit different long-term trends that are not related to the intrinsic variability of the source. As an illustration, we plot the same simulated light curves *A* and *B* with different added linear trends to simulate the effect of microlensing in Figure 3.

1.2. *Other time delay estimation methods.* Grid-based searches for time delay estimates are classic in this field. One-dimensional grid methods estimate the time delay, Δ_{AB} ,² between light curves *A* and *B* by minimizing the χ^2 distance or by maximizing the cross-correlation between two light curves, $\mathbf{x}(t)$ and $\mathbf{y}(t + \Delta_{AB})$, on a grid of values of Δ_{AB} (Fassnacht et al., 1999). Both techniques require an interpolation scheme. The dispersion method (Pelt et al., 1994) combines two light curves by shifting one of them in time and magnitude by Δ_{AB} and β_0 , respectively. This is called the *curve-shifting* assumption. The method estimates Δ_{AB} and β_0 on a two dimensional grid by minimizing the sum of squared differences between consecutive pairs of magnitudes on the combined curve. A bootstrapping method is used to produce standard errors of the time delay estimates. These methods account only for the intrinsic variability of a quasar. (When it is clear from the context, we suppress the subscript on Δ_{AB} and simply use Δ .)

Model-based methods have also been proposed in past to avoid the computational burden of evaluating the fit on a fine grid. For example, Tewes, Courbin and Meylan (2012) model the intrinsic and extrinsic variabilities of light curves using high-order and low-order splines, respectively. They obtain the least square estimate of Δ by iterating a two-step fitting routine in

²A positive value of Δ_{AB} indicates that features in light curve *A* appear before they appear in light curve *B*.

which splines are first fit given Δ and then Δ is optimized given the model fit. They also use a parametric bootstrapping for the standard error of the time delay estimate.

Harva and Raychaudhury (2006, hereafter H&R) introduced the first fully Bayesian approach, though they do not account for microlensing. They assume each observed light curve is generated by an unobserved underlying process. One of the latent processes is assumed to be a shifted and scaled version of the other, with the time and magnitude shifts and the magnitude scale treated as unknown parameters. They use a collapsed Gibbs-type sampler for model fitting, with the latent process integrated out of the target posterior distribution. Unlike other existing methods this approach unifies parameter estimation and uncertainty quantification into a single coherent analysis based on the posterior distribution of Δ .

1.3. *Our Bayesian and profile likelihood approaches.* The TDC motivated us to improve on H&R’s fully Bayesian model by taking advantage of modeling and computational advances made since H&R’s 2006 proposal. Specifically, we adopt an Ornstein-Uhlenbeck (O-U) process (Uhlenbeck and Ornstein, 1930) to model the latent light curve. The O-U process has been empirically shown to describe the stochastic variability of quasar data well (Kelly, Bechtold and Siemiginowska, 2009; Kozłowski et al., 2010; MacLeod et al., 2010; Zu et al., 2013). We address the effect of microlensing by incorporating a polynomial regression on time into the model. We specify scientifically motivated prior distributions and conduct a set of systematic sensitivity analyses. A Metropolis-Hastings (M-H) within Gibbs sampler (Tierney, 1994) is used to take advantage of the latent process rather than integrating it out as did H&R. We improve the convergence rate of our MCMC (Markov chain Monte Carlo) sampler by using an ancillarity-sufficiency interweaving strategy (Yu and Meng, 2011) and adaptive MCMC (Brooks et al., 2011).

To complement the Bayesian method, we introduce a simple profile likelihood approach that allows us to remove nuisance parameters and focus on Δ (e.g., Davison, 2003). We show that the profile likelihood function of Δ is approximately proportional to the marginal posterior distribution of Δ when a Jeffreys’ prior is used for the nuisance parameters (Berger et al., 1999), see Appendix D. For the problems we investigate the profile likelihood is nearly identical to the marginal posterior distribution, validating both methods.

Our time delay estimation strategy combines these two complementary approaches. We first obtain the profile likelihood of Δ , which is simple to compute. A more principled fully Bayesian analysis focuses on the dominant mode identified by the profile likelihood and provides joint inference for the

time delay and other model parameters via the joint posterior distribution.

The rest of this paper is organized as follows. We describe our Bayesian model in Section 2 and the MCMC sampler that we use to fit it in Section 3. In Section 4, we introduce the profile likelihood approach. We then specify our estimation strategy and illustrate it via a set of numerical examples in Section 5. An R package, `timedelay`, that implements the Bayesian and profile likelihood methods is publicly available at CRAN (<https://cran.r-project.org/package=timedelay>).

2. A fully Bayesian model for time delay estimation.

2.1. *Latent time series.* We assume that each time-delayed light curve is generated from a latent curve representing the true source magnitude in continuous time. For example, the solid red and dashed blue curves in Figure 4 are the latent light curves and are denoted by $\mathbf{X} = \{X(t), t \in \mathbf{R}\}$ and $\mathbf{Y} = \{Y(t), t \in \mathbf{R}\}$, respectively, where $X(t)$ and $Y(t)$ are unobserved true magnitudes at time t . We use the vector notation $\mathbf{X}(\mathbf{t}) = (X(t_1), X(t_2), \dots, X(t_n))^T$ and $\mathbf{Y}(\mathbf{t}) = (Y(t_1), Y(t_2), \dots, Y(t_n))^T$ to denote the n magnitudes of each latent light curve at the irregularly-spaced observation times \mathbf{t} .

A curve-shifted model (Pelt et al., 1994; Kochanek et al., 2006) assumes that one of the latent light curves is a shifted version of the other, that is

$$(2.1) \quad Y(t) = X(t - \Delta) + \beta_0,$$

where Δ is a shift in time and β_0 is a magnitude offset. For example, we generated the latent curves in Figure 4 under the model in (2.1). Thus the

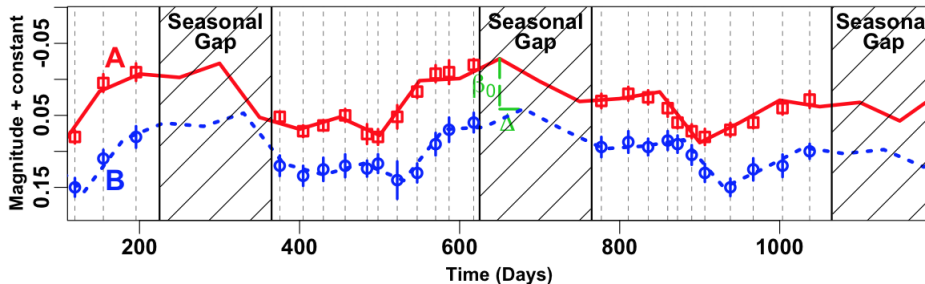


FIG 4. The dashed blue and solid red curves represent the latent continuous time light curves and are superimposed on Figure 2. The curve-shifted model in (2.1) specifies that the blue dashed curve is a shifted version of the red curve by Δ ($=70$) days in time and by β_0 ($=0.07$) in magnitude.

two latent curves exactly overlap if the solid red curve is shifted by Δ days and by β_0 magnitude units. The key advantage of this model is that a single latent light curve, here \mathbf{X} , is sufficient to represent the true magnitude time series of the two (or more) lensed images. This model is a special case of H&R’s scaled curve-shifted model, $Y(t) = sX(t - \Delta) + \beta_0$, where s is a magnitude scale change, mentioned at the end of Section 1.2. Setting $s = 1$ is reasonable because gravitational lensing only deflects the source light and magnifies it, i.e., multiplies the source flux. Because magnitude is on the \log_{10} scale of source flux, we expect an additive offset, i.e., β_0 , rather than a scale change. Since the curve-shifted model reflects gravitational lensing well, it is appropriate for estimating Δ , at least in the absence of microlensing.

Microlensing causes additional long-term extrinsic variability unrelated to the intrinsic quasar variability driving the dynamics of \mathbf{X} . Thus, the curve-shifted model is not appropriate in the presence of microlensing. To account for microlensing, we assume that one of the latent light curves is a time-shifted version of the other, but with an additional m -order polynomial regression on $t - \Delta$, that is

$$(2.2) \quad Y(t) = X(t - \Delta) + \mathbf{w}_m^\top(t - \Delta)\boldsymbol{\beta},$$

where $\mathbf{w}_m(t - \Delta) \equiv (1, t - \Delta, (t - \Delta)^2, \dots, (t - \Delta)^m)^\top$ is a covariate vector of length $m + 1$, and $\boldsymbol{\beta} \equiv (\beta_0, \beta_1, \beta_2, \dots, \beta_m)^\top$ is a vector of regression coefficients. The polynomial regression term in (2.2) accounts for the difference in the microlensing trends of the two light curves, i.e., the difference between the long-term trends of $Y(t)$ and $X(t - \Delta)$. The microlensing model in (2.2) reduces to a curve-shifted model in (2.1) if $\beta_1 = \beta_2 = \dots = \beta_m = 0$.

The best choice for the order of the polynomial regression depends on the extent of microlensing, and this varies from quasar to quasar. We set $m = 3$ as a default because the third order polynomial regression has been successfully applied to model lensed quasars (Kochanek et al., 2006; Tewes, Courbin and Meylan, 2012; Morgan et al., 2012). If we find evidence via the profile likelihood that a third order polynomial regression is not sufficient to reduce the effect of microlensing (see Section 5.1 for details), we can impose a reasonable upper bound of m by running preliminary regression on the observed light curves, and comparing the fits.

2.2. Distribution of the observed data. Observing the gravitationally-lensed images with a telescope, an astronomer measures the magnitude in each image, $x(t_j)$ and $y(t_j)$, along with the standard deviations, $\delta(t_j)$ and $\eta(t_j)$, at time t_j , $j = 1, 2, \dots, n$. We assume that these measurements have independent Gaussian errors centered at the latent magnitudes $X(t_j)$ and

$Y(t_j)$, i.e.,

$$(2.3) \quad x(t_j) | X(t_j) \stackrel{\text{indep.}}{\sim} \text{N}[X(t_j), \delta^2(t_j)],$$

$$(2.4) \quad y(t_j) | Y(t_j) \stackrel{\text{indep.}}{\sim} \text{N}[Y(t_j), \eta^2(t_j)],$$

where $\text{N}[M, V]$ is a Gaussian distribution with mean M and variance V , and $\mathbf{x}(\mathbf{t})$ and $\mathbf{y}(\mathbf{t})$ are independent given their true magnitudes. Using the model in (2.2), we can express (2.4) as

$$(2.5) \quad y(t_j) | X(t_j - \Delta), \Delta, \boldsymbol{\beta} \stackrel{\text{indep.}}{\sim} \text{N}[X(t_j - \Delta) + \mathbf{w}_m^\top(t_j - \Delta)\boldsymbol{\beta}, \eta^2(t_j)].$$

Given Δ , we define $\mathbf{t}^\Delta = (t_1^\Delta, t_2^\Delta, \dots, t_{2n}^\Delta)^\top$ as the sorted vector of $2n$ times among the n observation times, \mathbf{t} , and the n time-delay-shifted observation times, $\mathbf{t} - \Delta$. Also, $\mathbf{X}(\mathbf{t}^\Delta) = (X(t_1^\Delta), X(t_2^\Delta), \dots, X(t_{2n}^\Delta))^\top$ is the vector of $2n$ latent magnitudes at the times in \mathbf{t}^Δ . The joint density function of the observed data given $\mathbf{X}(\mathbf{t}^\Delta)$, Δ , and $\boldsymbol{\beta}$ is

$$(2.6) \quad p(\mathbf{x}(\mathbf{t}), \mathbf{y}(\mathbf{t}) | \mathbf{X}(\mathbf{t}^\Delta), \Delta, \boldsymbol{\beta}) = \prod_{j=1}^n p(x(t_j) | X(t_j)) \times p(y(t_j) | X(t_j - \Delta), \Delta, \boldsymbol{\beta}),$$

where the two distributions in the product are given in (2.3) and (2.5).

2.3. Distribution of the latent magnitudes. We assume the latent continuous time light curve, \mathbf{X} , is a realization of an O-U process (Uhlenbeck and Ornstein, 1930) as proposed in Kelly, Bechtold and Siemiginowska (2009, hereafter KBS). The stochastic differential equation,

$$(2.7) \quad dX(t) = -\frac{1}{\tau}(X(t) - \mu)dt + \sigma dB(t),$$

defines the O-U process, where μ and σ are on the magnitude scale and govern the overall mean and short-term variability of the underlying process, τ is a timescale (in days) for the process to revert to the long-term mean μ , $\{B(t), t \geq 0\}$ is a standard Brownian motion, and $dB(t)$ is an interval of the Brownian motion, whose distribution is Gaussian with mean zero and variance dt . We denote the three O-U parameters by $\boldsymbol{\theta} = (\mu, \sigma^2, \tau)^\top$.

KBS empirically demonstrated that the power spectrum of the O-U process is consistent with the mean power spectrum of 55 well-sampled quasar light curves at a specific frequency range with timescales shorter than τ . KBS also investigated the associations between model parameters and the physical properties of quasars. For example, τ has a positive correlation

with black hole mass, which is consistent with previous astrophysical studies. [Kozłowski et al. \(2010\)](#) and [MacLeod et al. \(2010\)](#) were concerned about a possible selection bias in the sample of quasars used in KBS and thus they analyzed thousands of light curves. [Kozłowski et al. \(2010\)](#) found further support for the O-U process in their analyses of about 2,700 quasars obtained from the Optical Gravitational Lensing Experiment (OGLE, [Kozłowski and Kochanek, 2009](#)). They showed that the distribution of the goodness of fit statistic obtained by fitting the O-U process to their light curves was consistent to the expected distribution of the statistic under the assumption that the light curve variation was stochastic. [MacLeod et al. \(2010\)](#) further verified the argument about the correlations between model parameters and physical properties in KBS by analyzing about 9,000 quasars obtained from the Sloan Digital Sky Survey ([Berk et al., 2004](#)). [Zu et al. \(2013\)](#) also supported the O-U process by comparing it to the Gaussian process with three different covariance functions in fitting about 200 OGLE light curves. Their numerical results based on the F -test and Bayesian information criterion supported the O-U process. These studies popularized the O-U process among astrophysicists to the extent that the TDC simulated its quasar light curves under an O-U process ([Dobler et al., 2015](#)). The earlier approach of H&R (2006) preceded these more recent advances in astrophysical and statistical modeling of quasars.

The solution of the stochastic differential equation in (2.7) provides the sampling distribution for the time-sorted latent magnitudes $\mathbf{X}(t^\Delta)$ via its Markovian property. Specifically,

$$(2.8) \quad X(t_1^\Delta) \mid \Delta, \boldsymbol{\theta} \sim \text{N} \left[\mu, \frac{\tau\sigma^2}{2} \right], \text{ and for } j = 2, 3, \dots, 2n,$$

$$X(t_j^\Delta) \mid X(t_{j-1}^\Delta), \Delta, \boldsymbol{\theta} \sim \text{N} \left[\mu + a_j(X(t_{j-1}^\Delta) - \mu), \frac{\tau\sigma^2}{2}(1 - a_j^2) \right],$$

where $a_j \equiv \exp(-(t_j^\Delta - t_{j-1}^\Delta)/\tau)$ is a shrinkage factor that depends on the observational cadence and τ . If two adjacent latent magnitudes are close in time, i.e., $t_j^\Delta - t_{j-1}^\Delta$ is small, a_j is close to one and $X(t_j^\Delta)$ borrows more information or shrinks more towards the previous latent magnitude, $X(t_{j-1}^\Delta)$, and exhibits less uncertainty. On the other hand, if neighboring latent magnitudes are distant in time, e.g., due to a seasonal gap, a_j is close to zero, and $X(t_j^\Delta)$ borrows little information from the distant value $X(t_{j-1}^\Delta)$ and instead approaches the overall mean μ . This is known as *mean reversion* property of the O-U process.

The joint density function of the $2n$ latent magnitudes is

$$(2.9) \quad p(\mathbf{X}(t^\Delta) \mid \Delta, \boldsymbol{\theta}) = p(X(t_1^\Delta) \mid \Delta, \boldsymbol{\theta}) \times \prod_{j=2}^{2n} p(X(t_j^\Delta) \mid X(t_{j-1}^\Delta), \Delta, \boldsymbol{\theta}),$$

where the distributions on the right-hand side are given in (2.8).

2.4. *Prior distributions for the time delay and the magnitude offset.* We adopt the proper prior distributions, for Δ and $\boldsymbol{\beta}$,

$$(2.10) \quad p(\Delta, \boldsymbol{\beta}) = p(\Delta)p(\boldsymbol{\beta}) \propto I_{\{u_1 \leq \Delta \leq u_2\}} \times N_{m+1}(\boldsymbol{\beta} \mid \mathbf{0}, 10^5 \times I_{m+1}),$$

where $I_{\{D\}}$ is the indicator function of D , $N_{m+1}(\boldsymbol{\beta} \mid \mathbf{0}, I_{m+1})$ is an $m + 1$ dimensional Gaussian density evaluated at $\boldsymbol{\beta}$ whose mean is $\mathbf{0}$, a vector of zeros with length $m + 1$, and variance-covariance matrix is $10^5 \times I_{m+1}$, with an $m + 1$ dimensional identity matrix I_{m+1} . We put a diffuse Gaussian prior on $\boldsymbol{\beta}$ to minimize impact on the posterior inference and to ensure posterior propriety.

The range of the uniform prior distribution on Δ , $[u_1, u_2]$, reflects the range of interest. One choice is the *entire feasible range* (or feasible range) of Δ , $[t_1 - t_n, t_n - t_1]$, where there is at least one data point that overlaps between the two light curves. Outside of this range, the two light curves do not overlap and the data cannot identify Δ . (H&R used a diffuse Gaussian prior distribution on Δ that was defined outside its feasible range.)

In some cases, information about the likely range of Δ is available from previous analyses or possibly from astrophysical probes. To find the likely range of Δ , we can also use a physical model for the mass and gravitational potential of the lens, as well as the redshifts (an astronomical measure of distance) and relative spatial locations of a quasar and lens.

2.5. *Prior distributions for the parameters in the O-U process.* Considering both scientific knowledge and the dynamics of the O-U process, we put a uniform distribution on the O-U mean μ , an independent inverse-Gamma (IG) distribution, $IG(1, b_\sigma)$, on its short-term variance σ^2 , and an independent $IG(1, 1)$ distribution on its timescale τ , i.e.,

$$(2.11) \quad p(\mu, \sigma^2, \tau) = p(\mu)p(\sigma^2)p(\tau) \propto \frac{\exp(-b_\sigma/\sigma^2)}{(\sigma^2)^2} \cdot \frac{\exp(-1/\tau)}{\tau^2} \\ \times I_{\{-30 \leq \mu \leq 30\}} \cdot I_{\{\sigma^2 > 0\}} \cdot I_{\{\tau > 0\}}.$$

Here the uniform distribution on μ encompasses a magnitude range from that of the Sun (magnitude = -26.74) to that of the faintest object visible

with the Hubble Space Telescope (magnitude = 30). The IG distributions on τ and σ^2 set their soft lower bounds³ to focus on practical solutions in which Δ can be constrained. For example, in the limits when τ is much less than the observation cadence or when σ^2 is much smaller than the measurement variance divided by the cadence, the discrete observations of the continuous latent light curve appear as serially uncorrelated white noise sequence. In these limiting cases it is impossible to estimate Δ by matching serially correlated fluctuation patterns. The soft lower bounds for τ and σ^2 discount these limiting cases, and allow us to focus on the relevant parameter space in which we expect time delay estimation to be feasible.

The relationship between the IG and scaled inverse- χ^2 distributions allows us to interpret the shape parameter of the IG as half the number of directly observed pseudo realizations of the O-U process that would carry equivalent information as the prior distribution. (See, e.g., [Gelman et al. \(2013\)](#) for a discussion of the pseudo observation interpretation of prior distributions.) Thus, we set the shape parameter of the IG prior on τ to one; this corresponds to two pseudo observations and can be interpreted as an indication that the prior distribution is relatively weak. It is practical to set the scale parameter of the IG prior for τ to one; the resulting soft lower bound on τ is 0.5 day and is smaller than all estimates of τ in [MacLeod et al. \(2010\)](#), who analyzed 9,275 quasars.

For the IG prior distribution of σ^2 , we set the shape parameter to one and the scale parameter⁴ to $(\text{Mean measurement standard error})^2 / (\text{Median cadence})$, i.e.,

$$(2.12) \quad b_\sigma = \frac{[\{\sum_{j=1}^n \delta(t_j) + \sum_{j=1}^n \eta(t_j)\}/2n]^2}{\text{Median}(t_2 - t_1, t_3 - t_2, \dots, t_n - t_{n-1})}.$$

This scale parameter enables us to search for solutions for which we can constrain Δ by avoiding the above limiting cases. Another viable choice for the scale parameter is $b_\sigma = 2/10^7$ because all estimates of σ^2 in [MacLeod et al. \(2010\)](#) are larger than this value. Sensitivity analyses for the choice of prior distributions of τ and σ^2 appear in [Appendix E](#).

3. Metropolis-Hastings within Gibbs sampler. Our overall hierarchical model is specified via the observation model in [\(2.3\)](#) and [\(2.5\)](#), the O-U process for the latent light curve in [\(2.8\)](#), and the prior distributions

³Because the density function of $\text{IG}(a, b)$ decreases exponentially from its mode, $b/(a+1)$, toward zero and geometrically decreases with a power of $a+1$ towards infinity, it is relatively unlikely for the random variable to take on values smaller than its mode.

⁴The physical unit of b_σ is magnitude squared per day, hereafter mag^2 per day.

given in (2.10) and (2.11). Our first approach to model fitting uses a Gibbs-type sampler to explore the resulting full posterior distribution. Instead of integrating out the latent magnitudes and using a collapsed sampler as H&R did, we treat $\mathbf{X}(\mathbf{t}^\Delta)$ as latent variables, alternatively updating $\mathbf{X}(\mathbf{t}^\Delta)$ and the other model parameters. (We could formulate our approach as data augmentation with $\mathbf{X}(\mathbf{t}^\Delta)$ as the missing data, see [van Dyk and Meng \(2001\)](#).)

Specifically, we use a Metropolis-Hastings within Gibbs (MHwG) sampler ([Tierney, 1994](#)) that iteratively samples five complete conditional distributions of the full joint posterior density, $p(\mathbf{X}(\mathbf{t}^\Delta), \Delta, \boldsymbol{\beta}, \boldsymbol{\theta} \mid \mathbf{x}(\mathbf{t}), \mathbf{y}(\mathbf{t}))$, proportional to the product of densities of observed and latent data in (2.6) and (2.9) and prior densities in (2.10) and (2.11). Iteration l of our sampler is composed of five steps.

$$(3.1) \text{ Step 1: Sample } (\mathbf{X}^{(l)}(\mathbf{t}^{\Delta^{(l)}}), \Delta^{(l)}) \sim p(\mathbf{X}(\mathbf{t}^\Delta), \Delta \mid \boldsymbol{\beta}^{(l-1)}, \boldsymbol{\theta}^{(l-1)}) \\ = p(\mathbf{X}(\mathbf{t}^\Delta) \mid \Delta, \boldsymbol{\beta}^{(l-1)}, \boldsymbol{\theta}^{(l-1)}) \times p(\Delta \mid \boldsymbol{\beta}^{(l-1)}, \boldsymbol{\theta}^{(l-1)}) \text{ by M-H}$$

$$(3.2) \text{ Step 2: Sample } \boldsymbol{\beta}^{(l)} \sim p(\boldsymbol{\beta} \mid \boldsymbol{\theta}^{(l-1)}, \mathbf{X}^{(l)}(\mathbf{t}^{\Delta^{(l)}}), \Delta^{(l)})$$

$$(3.3) \text{ Step 3: Sample } \mu^{(l)} \sim p(\mu \mid (\sigma^2)^{(l-1)}, \tau^{(l-1)}, \mathbf{X}^{(l)}(\mathbf{t}^{\Delta^{(l)}}), \Delta^{(l)}, \boldsymbol{\beta}^{(l)})$$

$$(3.4) \text{ Step 4: Sample } (\sigma^2)^{(l)} \sim p(\sigma^2 \mid \tau^{(l-1)}, \mathbf{X}^{(l)}(\mathbf{t}^{\Delta^{(l)}}), \Delta^{(l)}, \boldsymbol{\beta}^{(l)}, \mu^{(l)})$$

$$(3.5) \text{ Step 5: Sample } \tau^{(l)} \sim p(\tau \mid \mathbf{X}^{(l)}(\mathbf{t}^{\Delta^{(l)}}), \Delta^{(l)}, \boldsymbol{\beta}^{(l)}, \mu^{(l)}, (\sigma^2)^{(l)}) \text{ by M-H,}$$

where we suppress conditioning on $\mathbf{x}(\mathbf{t})$ and $\mathbf{y}(\mathbf{t})$ in all five steps. The conditional distributions in (3.2), (3.3), and (3.4), are standard families that can be sampled directly, whereas those in (3.1) and (3.5) require M-H updates. We use the factorization in (3.1) to construct a joint proposal, $(\tilde{\mathbf{X}}(\mathbf{t}^{\tilde{\Delta}}), \tilde{\Delta})$, for $(\mathbf{X}(\mathbf{t}^\Delta), \Delta)$ and calculate its acceptance probability. First, $\tilde{\Delta}$ is proposed from the Gaussian density $N(\Delta^{(l-1)}, \psi^2)$, where ψ is a proposal scale and is set to produce a reasonable acceptance rate. Given $\tilde{\Delta}$, we propose $\tilde{\mathbf{X}}(\mathbf{t}^{\tilde{\Delta}}) \sim p(\mathbf{X}(\mathbf{t}^{\tilde{\Delta}}) \mid \tilde{\Delta}, \boldsymbol{\beta}^{(l-1)}, \boldsymbol{\theta}^{(l-1)}, \mathbf{x}(\mathbf{t}), \mathbf{y}(\mathbf{t}))$; this is a Gaussian distribution and is specified in Appendix A. Because the proposal for Δ and that for $\mathbf{X}(\mathbf{t}^\Delta)$ given Δ are symmetric, $(\tilde{\mathbf{X}}(\mathbf{t}^{\tilde{\Delta}}), \tilde{\Delta})$ is accepted with a probability $\min(1, r)$, where

$$(3.6) \quad r = \frac{p(\tilde{\Delta} \mid \boldsymbol{\beta}^{(l-1)}, \boldsymbol{\theta}^{(l-1)}, \mathbf{x}(\mathbf{t}), \mathbf{y}(\mathbf{t}))}{p(\Delta^{(l-1)} \mid \boldsymbol{\beta}^{(l-1)}, \boldsymbol{\theta}^{(l-1)}, \mathbf{x}(\mathbf{t}), \mathbf{y}(\mathbf{t}))}.$$

Details of the marginalized density $p(\Delta \mid \boldsymbol{\beta}, \boldsymbol{\theta}, \mathbf{x}(\mathbf{t}), \mathbf{y}(\mathbf{t}))$ in (3.6) appear in Appendix B and details of Step 2–5 appear in Appendix C.

The direct updates for $\boldsymbol{\beta}$, μ , and σ^2 are based on standard families that are not available under H&R’s collapsed approach. Thus the collapsed approach

must update each of the model parameters via a Metropolis or M-H update, which can slow down the rate of convergence. (Collapsing Gibbs-type samplers, however, is known to improve their rate of convergence (Liu, 2008) if the complete conditionals can be sampled directly.) Also, the collapsed MHwG (CMHwG) sampler requires about three times more CPU time per iteration than the (non-collapsed) MHwG sampler that we propose. In Figure 5, we compare the autocorrelation functions (ACFs) of Δ , β_0 , μ , σ^2 , and τ obtained by the CMHwG sampler (first row) and those obtained by our MHwG sampler (second row). The sampler in the third row is discussed in Section 3.1. All algorithms are run using the curve-shifted model in (2.1) fit to data for quasar *Q0957+561* (Hainline et al., 2012). Except for that of β_0 , the ACFs generated with CMHwG (first row), decay slower than those obtained with MHwG (second row). The effective sample sizes per second (ESS/sec) tend to improve with MHwG over CMHwG. For example, for Δ the ESS/sec is 5.23 with CMHwG and 21.09 with MHwG. The exception is β_0 , for which ESS/sec is 6.33 with CMHwG, but only 1.74 with MHwG. In the following section, we discuss a way to improve the convergence rate of β_0 (β in general) for the MHwG sampler, while retaining its fast running time.

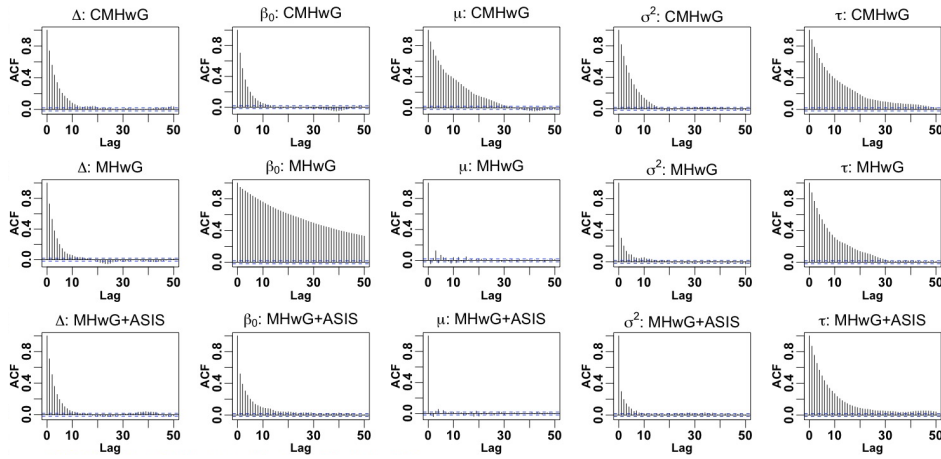


FIG 5. The autocorrelation functions for $\Delta, \beta_0, \mu, \sigma^2$, and τ (columns from left to right) based on 10,000 posterior samples after a burn-in of 10,000. Results are obtained using three different posterior samplers (CMHwG, MHwG, and MHwG + ASIS, rows from top to bottom). We use the curve-shifted model for simplicity and the data from quasar *Q0957+671* analyzed in Section 5.3.

3.1. *Ancillarity-sufficiency interweaving strategy.* To improve the convergence rate of β , we adopt the ancillarity-sufficiency interweaving strategy (ASIS, Yu and Meng, 2011). ASIS interweaves trajectories of Markov chains of β obtained by two discordant parameterizations of the unknown quantities. The two parameterizations are designed so that the latent variables can be viewed as ancillary and sufficient statistics for β , respectively.

In the parameterization used up until now, $\mathbf{X}(\mathbf{t}^\Delta)$ is an *ancillary augmentation* (AA) for β in that it is an ancillary statistic for β . That is, the distribution of $\mathbf{X}(\mathbf{t}^\Delta)$ in (2.8) does not depend on β . On the other hand, a *sufficiency augmentation* (SA) for β is based on the latent variables that have sufficient information to estimate β , that is, a sufficient statistic for β . To derive a SA for β , we introduce the parameterization,

$$(3.7) \quad K(t_j^\Delta) \equiv X(t_j^\Delta) + \mathbf{w}_m^\top(t_j^\Delta)\beta \cdot I_{\mathbf{t}-\Delta}(t_j^\Delta), \text{ for } j = 1, 2, \dots, 2n,$$

where

$$(3.8) \quad I_{\mathbf{t}-\Delta}(t_j^\Delta) = \begin{cases} 1, & \text{if } t_j^\Delta \in \mathbf{t} - \Delta, \\ 0, & \text{if } t_j^\Delta \in \mathbf{t}. \end{cases}$$

This indicator is one if t_j^Δ is an element of $\mathbf{t} - \Delta = \{t_1 - \Delta, t_2 - \Delta, \dots, t_n - \Delta\}$ and zero otherwise. Using (3.7), we express the observation model in (2.3) and (2.5) as

$$(3.9) \quad x(t_j) | K(t_j) \stackrel{\text{indep.}}{\sim} \text{N}[K(t_j), \delta^2(t_j)].$$

$$(3.10) \quad y(t_j) | K(t_j - \Delta), \Delta \stackrel{\text{indep.}}{\sim} \text{N}[K(t_j - \Delta), \eta^2(t_j)].$$

The distributions of latent light curve in (2.8) is replaced by

$$(3.11) \quad \begin{aligned} K(t_1^\Delta) | \Delta, \beta, \theta &\sim \text{N}\left[\mu + \mathbf{w}_m^\top(t_1^\Delta)\beta \cdot I_{\{\mathbf{t}-\Delta\}}(t_1^\Delta), \frac{\tau\sigma^2}{2}\right], \\ K(t_j^\Delta) | K(t_{j-1}^\Delta), \Delta, \beta, \theta &\sim \text{N}\left[\mu + \mathbf{w}_m^\top(t_j^\Delta)\beta \cdot I_{\{\mathbf{t}-\Delta\}}(t_j^\Delta) \right. \\ &\quad \left. + a_j(K(t_{j-1}^\Delta) - \mu - \mathbf{w}_m^\top(t_{j-1}^\Delta)\beta \cdot I_{\{\mathbf{t}-\Delta\}}(t_{j-1}^\Delta)), \frac{\tau\sigma^2}{2}(1 - a_j^2)\right]. \end{aligned}$$

Under this reparameterization of the model in terms of $\mathbf{K}(\mathbf{t}^\Delta)$, β appears only in (3.11), which means that $\mathbf{K}(\mathbf{t}^\Delta)$ contain sufficient information to estimate β and thus $\mathbf{K}(\mathbf{t}^\Delta)$ is SA for β . Because the parameterization does not affect the prior distributions of the model parameters in (2.10) and (2.11), the full joint posterior density in terms of $\mathbf{K}(\mathbf{t}^\Delta)$,

i.e., $p(\mathbf{K}(\mathbf{t}^\Delta), \Delta, \boldsymbol{\beta}, \boldsymbol{\theta} \mid \mathbf{x}(\mathbf{t}), \mathbf{y}(\mathbf{t}))$, is proportional to the product of densities of observed and latent data, whose distributions are specified in (3.9), (3.10), and (3.11), and prior densities in (2.10) and (2.11). Consequently, the marginal posterior distribution of the model parameters, $\{\Delta, \boldsymbol{\beta}, \boldsymbol{\theta}\}$, is unchanged.

ASIS interweaves the trajectory of $\boldsymbol{\beta}$ from a sample constructed under AA and that constructed under SA. This can be accomplished by replacing Step 2 in (3.2) with the following four steps:

$$(3.12) \quad \text{Step } 2_a : \text{ Sample } \boldsymbol{\beta}_{\text{AA}}^{(l)} \sim p(\boldsymbol{\beta} \mid \boldsymbol{\theta}^{(l-1)}, \mathbf{X}^{(l)}(\mathbf{t}^{\Delta^{(l)}}), \Delta^{(l)})$$

$$(3.13) \quad \text{Step } 2_b : \text{ Set } K^{(l)}(t_j^{\Delta^{(l)}}) = X^{(l)}(t_j^{\Delta^{(l)}}) + \mathbf{w}_m^\top(t_j^{\Delta^{(l)}}) \boldsymbol{\beta}_{\text{AA}}^{(l)} I_{t-\Delta^{(l)}}(t_j^{\Delta^{(l)}})$$

$$(3.14) \quad \text{Step } 2_c : \text{ Sample } \boldsymbol{\beta}_{\text{SA}}^{(l)} \sim p(\boldsymbol{\beta} \mid \boldsymbol{\theta}^{(l-1)}, \mathbf{K}^{(l)}(\mathbf{t}^{\Delta^{(l)}}), \Delta^{(l)})$$

$$(3.15) \quad \text{Step } 2_d : \text{ Set } X^{(l)}(t_j^{\Delta^{(l)}}) = K^{(l)}(t_j^{\Delta^{(l)}}) - \mathbf{w}_m^\top(t_j^{\Delta^{(l)}}) \boldsymbol{\beta}_{\text{SA}}^{(l)} I_{t-\Delta^{(l)}}(t_j^{\Delta^{(l)}})$$

Again, we suppress the condition on $\mathbf{x}(\mathbf{t})$ and $\mathbf{y}(\mathbf{t})$. In Step 2_c, we set $\boldsymbol{\beta}^{(l)}$ to $\boldsymbol{\beta}_{\text{SA}}^{(l)}$ sampled from its conditional posterior distribution specified in (C.5). In Step 2_d, ASIS updates the latent variables, $\mathbf{X}^{(l)}(\mathbf{t}^{\Delta^{(l)}})$, to adjust for the inconsistency between the updates sampled in (3.3)–(3.5) that are based on the $\mathbf{X}^{(l)}(\mathbf{t}^{\Delta^{(l)}})$ and the update $\boldsymbol{\beta}^{(l)}$ that is based on $\mathbf{K}^{(l)}(\mathbf{t}^{\Delta^{(l)}})$. Updating $\mathbf{X}^{(l)}(\mathbf{t}^{\Delta^{(l)}})$ in (3.15) synchronizes this inconsistency and preserves the stationary distribution (Yu and Meng, 2011). The additional computational cost of ASIS is negligible because the conditional updates in (3.12) and (3.14) include quick multivariate Gaussian sampling, see Appendix (C.1) and (C.5) for details.

ACFs of the model parameters obtained by MHwG equipped with ASIS, denoted by MHwG+ASIS, appear on the third row of Figure 5; the ACF of β_0 in the second column shows a noticeable improvement compared to that obtained by MHwG sampler. The ESS/sec for β_0 is 20.95 with MHwG+ASIS and 1.74 with MHwG. (The ESS/sec for Δ is 21.35 with MHwG+ASIS and 21.09 with MHwG.)

3.2. Adaptive MCMC. Our MHwG sampler (either with or without ASIS) requires a proposal distribution in each of its two Metropolis steps, that is, $N[\Delta^{(l-1)}, \psi^2]$ used to update $\Delta^{(l)}$ in (3.1) and $N[\log(\tau^{(l-1)}), \phi^2]$ used to update $\log(\tau^{(l)})$ in (3.5), where ψ and ϕ are the proposal scales. To avoid burdensome off-line tuning of the proposal scales, we implement an adaptive MCMC (Brooks et al., 2011) that allows automatical adjustment during the run. We implement an algorithm that updates the two proposal

Set $\mathbf{X}^{(0)}(\mathbf{t}^{\Delta^{(0)}})$, $\Delta^{(0)}$, $\boldsymbol{\beta}^{(0)}$, $\boldsymbol{\mu}^{(0)}$, $(\sigma^2)^{(0)}$, $\tau^{(0)}$, $\psi^{(0)}$, $\phi^{(0)}$.
 For $l = 1, 2, \dots$
 Step 1: Sample $\Delta^{(l)}$ using a Metropolis step with proposal rule $N[\Delta^{(l-1)}, (\psi^{(l-1)})^2]$.
 If a new proposal for $\Delta^{(l)}$ is accepted, then sample $\mathbf{X}^{(l)}(\mathbf{t}^{\Delta^{(l)}})$,
 or otherwise set $\mathbf{X}^{(l)}(\mathbf{t}^{\Delta^{(l)}})$ to $\mathbf{X}^{(l-1)}(\mathbf{t}^{\Delta^{(l-1)}})$.
 Step 2: (ASIS) Update $\boldsymbol{\beta}^{(l)}$ and $\mathbf{X}^{(l)}(\mathbf{t}^{\Delta^{(l)}})$ via (3.12)–(3.15).
 Step 3: Sample $\boldsymbol{\mu}^{(l)}$ via (3.3).
 Step 4: Sample $(\sigma^2)^{(l)}$ via (3.4).
 Step 5: Sample $\tau^{(l)}$ using a M-H step with proposal rule $N[\log(\tau^{(l-1)}), (\phi^{(l-1)})^2]$.
 Step 6: (Adaptation) If $l \bmod 100 = 0$
 if the acceptance rate of Δ in iterations $l - 99, l - 98, \dots, l > 0.44$ **then**
 $\psi^{(l)} \leftarrow \psi^{(l-1)} \times \exp(\min(0.01, 1/\sqrt{(l/100)}))$
 else if the acceptance rate of Δ in iterations $l - 99, l - 98, \dots, l < 0.23$ **then**
 $\psi^{(l)} \leftarrow \psi^{(l-1)} \times \exp(-\min(0.01, 1/\sqrt{(l/100)}))$
 end if
 if the acceptance rate of τ in iterations $l - 99, l - 98, \dots, l > 0.44$ **then**
 $\phi^{(l)} \leftarrow \phi^{(l-1)} \times \exp(\min(0.01, 1/\sqrt{(l/100)}))$
 else if the acceptance rate of τ in iterations $l - 99, l - 98, \dots, l < 0.23$ **then**
 $\phi^{(l)} \leftarrow \phi^{(l-1)} \times \exp(-\min(0.01, 1/\sqrt{(l/100)}))$
 end if
 Otherwise $\psi^{(l)} = \psi^{(l-1)}$ and $\phi^{(l)} = \phi^{(l-1)}$.

FIG 6. Steps of the adaptive MHwG+ASIS sampler.

scales every 100 iterations, based on the most recent 100 proposals as outlined in Step 6 of Figure 6. The Markov chains equipped with the adaptive MCMC converge to the stationary distribution because the adjustment factors, $\exp(\pm \min(0.01, 1/\sqrt{i}))$, in Step 6 of of Figure 6 approach one as i goes to infinity. This condition is called diminishing adaptation condition (Roberts and Rosenthal, 2007). We set the lower and upper bounds of the acceptance rate to 0.23 and 0.44, respectively (Gelman et al., 2013).

The steps of the adaptive MHwG+ASIS sampler are specified in Figure 6. We describe our choice of initial values of the parameters in Section 5 as a part of our time delay estimation strategy.

4. Profile likelihood of the time delay. A profile likelihood of Δ (e.g., Davison, 2003) is a simple approximation to the marginal posterior distribution of Δ , $p(\Delta \mid \mathbf{x}(\mathbf{t}), \mathbf{y}(\mathbf{t}))$. It is defined as

$$(4.1) \quad L_{\text{prof}}(\Delta) \equiv \max_{\boldsymbol{\beta}, \boldsymbol{\theta}} L(\Delta, \boldsymbol{\beta}, \boldsymbol{\theta}) = L(\Delta, \hat{\boldsymbol{\beta}}_{\Delta}, \hat{\boldsymbol{\theta}}_{\Delta}),$$

where $L(\Delta, \boldsymbol{\beta}, \boldsymbol{\theta})$ is the likelihood function of the model parameters, that is,

(4.2)

$$\begin{aligned} L(\Delta, \boldsymbol{\beta}, \boldsymbol{\theta}) &= p(\mathbf{x}(\mathbf{t}), \mathbf{y}(\mathbf{t}) \mid \Delta, \boldsymbol{\beta}, \boldsymbol{\theta}) \\ &= \int p(\mathbf{x}(\mathbf{t}), \mathbf{y}(\mathbf{t}) \mid \mathbf{X}(\mathbf{t}^\Delta), \Delta, \boldsymbol{\beta}) \times p(\mathbf{X}(\mathbf{t}^\Delta) \mid \Delta, \boldsymbol{\theta}) d\mathbf{X}(\mathbf{t}^\Delta), \end{aligned}$$

and $(\hat{\boldsymbol{\beta}}_\Delta, \hat{\boldsymbol{\theta}}_\Delta)$ are the values of $(\boldsymbol{\beta}, \boldsymbol{\theta})$ that maximize $L(\Delta, \boldsymbol{\beta}, \boldsymbol{\theta})$ for each Δ .

In regular problems the profile likelihood of a parameter, say φ , approximates its marginal posterior distribution with a uniform prior on φ . This happens, for example, if the log likelihood of the model parameters is approximately quadratic given φ under standard asymptotic arguments. The prior distribution on the parameters other than φ is chosen in such a way as to approximately overset the variance term of the log likelihood, e.g., as happens asymptotically with the Jeffreys' prior, see Appendix D for details.

Treating $L_{\text{prof}}(\Delta)$ as an approximation to $p(\Delta \mid \mathbf{x}(\mathbf{t}), \mathbf{y}(\mathbf{t}))$, we evaluate $L_{\text{prof}}(\Delta)$ on a fine grid of values over the interesting range of Δ , $\{\Delta_1, \Delta_2, \dots, \Delta_w\}$. We set $\Delta_j - \Delta_{j-1} = 0.1$ ($j = 2, 3, \dots, w$) for a high-resolution mapping although this can be computationally burdensome due to the large number of values on the grid. For example, if the feasible range for Δ is $[-1500, 1500]$, the grid consists of 30,001 values. At one second per evaluation this requires about 8 hours and 20 minutes. Though computationally expensive, the high-resolution mapping of $L_{\text{prof}}(\Delta)$ is useful because it clearly identifies the likely (modal) values of Δ . In practice, we use multiple cores in parallel to reduce the computation time.

The profile likelihood evaluated on the grid can be used to approximate the posterior mean $E(\Delta \mid \mathbf{x}(\mathbf{t}), \mathbf{y}(\mathbf{t}))$ by

$$(4.3) \quad \hat{\Delta}_{\text{mean}} \equiv \frac{\sum_{j=1}^w \Delta_j \times L_{\text{prof}}(\Delta_j)}{\sum_{j=1}^w L_{\text{prof}}(\Delta_j)},$$

and the posterior variance $\text{Var}(\Delta \mid \mathbf{x}(\mathbf{t}), \mathbf{y}(\mathbf{t}))$ by

$$(4.4) \quad \hat{V} \equiv \frac{\sum_{j=1}^w \Delta_j^2 \times L_{\text{prof}}(\Delta_j)}{\sum_{j=1}^w L_{\text{prof}}(\Delta_j)} - \left[\frac{\sum_{j=1}^w \Delta_j \times L_{\text{prof}}(\Delta_j)}{\sum_{j=1}^w L_{\text{prof}}(\Delta_j)} \right]^2.$$

Moreover, the posterior mode of Δ can be approximated by a value of Δ in the grid that maximizes the profile likelihood, which is a discrete approximation to the maximum likelihood estimator, $\hat{\Delta}_{\text{MLE}} \equiv \arg \max_{\Delta} L_{\text{prof}}(\Delta)$.

5. Time delay estimation strategy and numerical illustrations.

The first step of our analysis is to plot $L_{\text{prof}}(\Delta)$ over the range of Δ to check for multimodality that may indicate multiple modes in the marginal posterior distribution of Δ . For some quasars, the interesting range of Δ can be narrowed using the results of past analyses or information from other astrophysical probes. If prior information for Δ is unavailable, we explore the feasible range.

In our numerical studies, we find that when $L_{\text{prof}}(\Delta)$ is unimodal, the moment estimates of Δ based on $L_{\text{prof}}(\Delta)$, i.e., $\hat{\Delta}_{\text{mean}}$ in (4.3) and \hat{V} in (4.4), are almost identical to the posterior mean and variance obtained via MCMC. On the other hand, modes near the margins of the range of Δ may indicate microlensing, see Section 5.1. In this case, the order of polynomial regression must be increased. If there are multiple modes, but they are not near the margins of the range, each mode merits investigation.

As a cross-check, we run three MCMC chains near the major mode(s) identified by $L_{\text{prof}}(\Delta)$. The three starting values for each mode are {mode, mode \pm 20 days}. Each chain is run for 20,000 iterations and the first 10,000 iterations are discarded as burn-in. For all chains, we set the starting value of β to the estimated regression coefficients obtained by regressing $\mathbf{y}(\mathbf{t}) - \sum_j x(t_j)/n$ on a covariate matrix $\mathbf{W}_m(\mathbf{t} - \Delta^{(0)})$ whose j th row is $W_m^\top(t_j - \Delta^{(0)})$, where $\Delta^{(0)}$ is the initial value of Δ . The initial value of $\mathbf{X}(\mathbf{t}^\Delta)$ is the combined light curve, that is, $\{\mathbf{x}(\mathbf{t}), \mathbf{y}(\mathbf{t} - \Delta^{(0)}) - \mathbf{W}_m^\top(\mathbf{t} - \Delta^{(0)})\beta^{(0)}\}$ sorted in time. The starting value of μ is set to the mean of $\mathbf{x}(\mathbf{t})$, that of σ^2 to 0.01^2 , and that of τ to 200. We set the initial standard deviations of the proposal distributions as $\psi = 10$ and $\phi = 3$.

We use simulated data of doubly- and quadruply-lensed quasars publicly available at the TDC website (<http://timedelaychallenge.org>) to illustrate our time delay estimation strategy when prior information for Δ is not available. We also analyze observed data of quasars *Q0957+561* and *J1029+2623* over the feasible range of Δ for illustrative purpose, though prior information is available to limit the range of Δ .

We report the CPU time in second using a server equipped with two 8-core Intel Xeon E5-2690 at 2.9 GHz and 64 GB of memory. We report the entire mapping time for $L_{\text{prof}}(\Delta)$.

5.1. *A doubly-lensed quasar simulation.* The simulated data for a doubly-lensed quasar are plotted in the first panel of Figure 7; the median cadence is 3 days, the cadence standard deviation is 1 day, and observations are made for 4 months in each of 5 years for 200 observations in total. The light curves suffer from microlensing which can be identified from their different

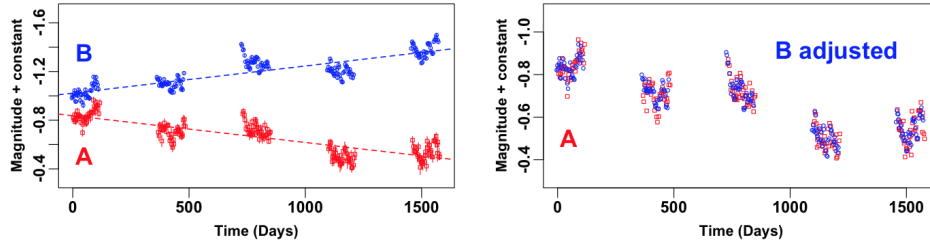


FIG 7. The first panel shows a TDC data set suffering from microlensing that results in light curves with different long-term trends. The dashed lines denote fitted linear regression lines. In the second panel, we shift light curve B by $\hat{\Delta}_{MLE}$ in the x-axis and subtract the estimated third-order polynomial regression from light curve B (using the values of β that maximize the profile likelihood at $\hat{\Delta}_{MLE}$). The microlensing model finds matches between the intrinsic fluctuations of the light curves after removing the relative microlensing trend from light curve B.

long-term linear trends and similar short-term (intrinsic) variability.

To show the effect of microlensing on the time delay estimation, we fit both the curve-shifted model ($m = 0$) in (2.1) and the microlensing model with $m = 3$ in (2.2). We plot $\log(L_{\text{prof}}(\Delta))$ and $L_{\text{prof}}(\Delta)$ base on the curve-shifted model over the feasible range, $[t_1 - t_n, t_n - t_1] = [-1575.85, 1575.85]$, in the two panels of Figure 8. The profile likelihood exhibits large modes near the margins that overwhelm the profile likelihood near the true time delay (5.86 days denoted by the vertical red dashed line).

In the presence of microlensing, the curve-shifted model cannot identify the time delay because the latent curves are not shifted versions of each other. The modes of $L_{\text{prof}}(\Delta)$ near the margins of the range of Δ occur

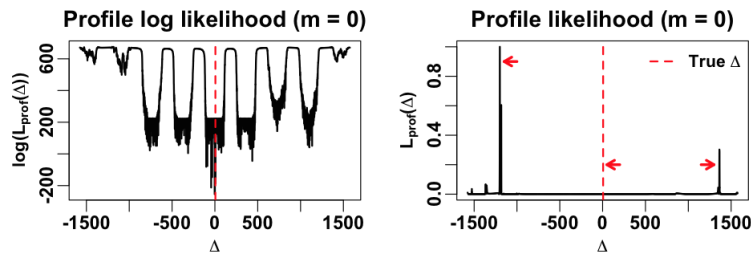


FIG 8. The profile log likelihood (left) and the profile likelihood (right) of Δ over its feasible range under the curve-shifted model ($m = 0$). We exponentiate $\log(L_{\text{prof}}(\Delta))$, setting the largest value of $L_{\text{prof}}(\Delta)$ to one. The vertical red dashed line indicates the true time delay. The profile likelihood near the true time delay (5.86 days) is overwhelmed by the modes near margins.

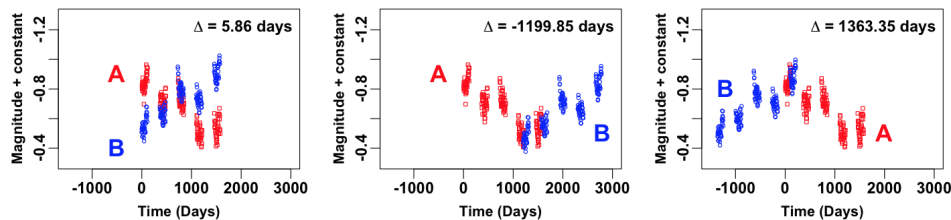


FIG 9. We shift light curve B (blue) by the true time delay (5.86 days) in the first panel, by $-1,199.85$ days in the second panel, and by 1363.35 days in the third panel. These three time delays correspond to three arrows in the second panel of Figure 8. The shift in magnitude used is the value of β_0 that maximizes the profile likelihood given each time delay. Without accounting for microlensing, the curve-shifted model fails because the light curves do not match even at the true time delay. The curve-shifted model may produce large modes near the margins because a small overlap between the tips of two light curves may have the only similar fluctuation patterns detectable by shifting one of the light curves as shown in the second and third panels.

because a small overlap between the tips of two light curves may exhibit the only similar fluctuation patterns detectable by shifting one of the light curves. In Figure 9, for instance, we shift light curve B in the x -axis by the three values of Δ indicated by three arrows in the second panel of Figure 8. In the first panel of Figure 9, the two light curves shifted by the true time delay do not match for any shift in magnitude. However, given the time delays at around $-1,200$ and $1,360$ days, the two light curves look well-connected as shown in the second and third panels. Thus, the profile likelihood near the true time delay is overwhelmed by the values of the profile likelihood near $-1,200$ and $1,360$ days.

To correct this effect, we fit the microlensing model with a third-order

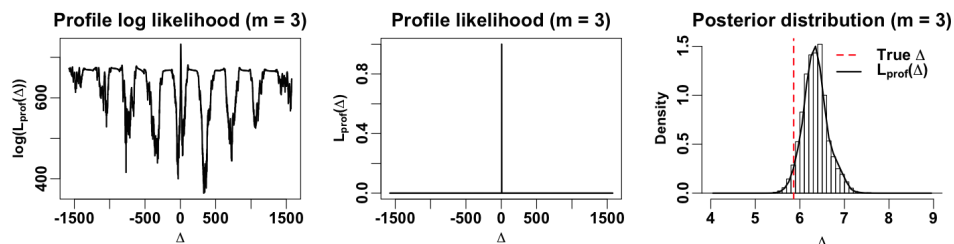


FIG 10. The profile log likelihood (first panel) and the profile likelihood (second panel) of Δ over its feasible range under the microlensing model ($m = 3$). The profile likelihood shows one mode near the true time delay (5.86 days). The third panel shows the marginal posterior distribution of Δ as a histogram of the MCMC samples with $L_{\text{prof}}(\Delta)$ superimposed. The vertical red dashed line indicates the true time delay.

TABLE 1

Estimates of Δ ; the profile likelihood estimates, $\hat{\Delta}_{\text{mean}}$ and $\hat{V}^{0.5}$ are given in the $E(\Delta|\mathbf{x}(\mathbf{t}), \mathbf{y}(\mathbf{t}))$ and $SD \equiv SD(\Delta|\mathbf{x}(\mathbf{t}), \mathbf{y}(\mathbf{t}))$ columns, where $\text{Error} \equiv |\Delta_{\text{true}} - E(\Delta|\mathbf{x}(\mathbf{t}), \mathbf{y}(\mathbf{t}))|$ with Δ_{true} indicating the true time delay (5.86 days), and $\chi \equiv \text{Error}/SD(\Delta|\mathbf{x}(\mathbf{t}), \mathbf{y}(\mathbf{t}))$.

Method	$E(\Delta D_{\text{obs}})$	$\hat{\Delta}_{\text{MLE}}$	SD	Δ_{true}	Error	χ
Bayesian	6.34		0.28	5.86	0.48	1.71
Profile likelihood	6.36	6.35	0.28	5.86	0.50	1.76

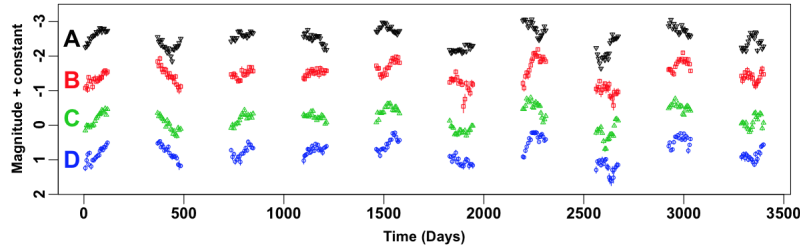
polynomial regression ($m = 3$). Both $\log(L_{\text{prof}}(\Delta))$ and $L_{\text{prof}}(\Delta)$ are plotted in Figure 10. One mode clearly dominates $L_{\text{prof}}(\Delta)$ and $\hat{\Delta}_{\text{mean}} = 6.36$ days. Using a uniform prior for Δ over its feasible range and $\sigma^2 \sim \text{IG}(1, 2/10^7)$, we initialize three MCMC chains near 6.36 days. We check the convergence with the Gelman-Rubin diagnostic statistic (GRD, Gelman and Rubin, 1992) which equals 1.0007 for Δ . It took 14,457 seconds to map $L_{\text{prof}}(\Delta)$ and 186 seconds on average for each MCMC chain. The profile likelihood and marginal posterior near the dominant mode are almost identical and are consistent with the true value of Δ as shown in the third panel of Figure 10.

In the second panel of Figure 7, we shift light curve B by $\hat{\Delta}_{\text{MLE}}$ (x -axis) and subtract the estimated polynomial regression (using the values of β that maximize $L_{\text{prof}}(\Delta)$ evaluated at $\hat{\Delta}_{\text{MLE}}$). The microlensing model finds matches between the intrinsic fluctuations of the light curves after removing the relative microlensing trend from light curve B .

We summarize the Bayesian and profile likelihood estimates for Δ in Table 1. The true delay is within two posterior standard deviation ($\chi \leq 1.76$) of the posterior mean; similar accuracy is obtained with the profile likelihood approximation.

5.2. *A quadruply-lensed quasar simulation.* The simulated data for a quadruply-lensed quasar are plotted in Figure 11 and are composed of four light curves, A, B, C , and D ; the median cadence is 6 days, the cadence standard deviation is 1 day, and observations are made for 4 months in each of 10 years with 200 observations in total. The feasible range for each Δ is $[-3391.62, 3391.62]$.

With quadruply lensed data there are six time delay parameters, one for each pair of light curves. Any three of these parameters determine the others and we focus on Δ_{AB} , Δ_{AC} , and Δ_{AD} , where the subscripts index the two light curves being compared. This pair-wise approach proceeds by applying the method developed for doubly-lensed data in Section 5.1 to the pair of light curves corresponding to each of Δ_{AB} , Δ_{AC} , and Δ_{AD} in turn (Fassnacht et al., 1999; Tewes, Courbin and Meylan, 2012).


 FIG 11. *Simulated quadruply-lensed quasar data used in the TDC.*

A coherent model would consider all four time series data in one model simultaneously (Hojjati, Kim and Linder, 2013); four time series are generated from one underlying true process and the three distinct time delays may have a posteriori correlations. By focusing on pairwise comparisons of the four time series, we do not account for the correlations between the time delays. Extending our model to simultaneously consider all of the data is a topic for future research.

We follow our default strategy to analyze these simulated data, using the microlensing model ($m = 3$). After confirming a single dominating mode in the profile likelihood for each time delay parameter, we initiate three MCMC chains near this mode; the GRD is 1.0000 for Δ_{AB} , 1.0010 for Δ_{AC} , and 1.0001 for Δ_{AD} . The posterior distributions of Δ_{AB} , Δ_{AC} , and Δ_{AD} appear in Figure 12 with $L_{\text{prof}}(\Delta)$ superimposed. The profile likelihood is almost identical to the posterior distribution of each parameter and both estimate the true time delays well. The average CPU time taken to map $L_{\text{prof}}(\Delta)$ is about 73,000 seconds (averaging over the three time delays). The average CPU time taken for each MCMC chain is about 200 seconds (averaging over nine chains; three chains for each time delay). Our estimation results

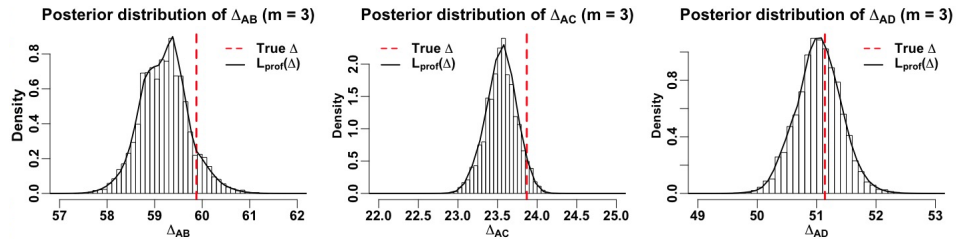

 FIG 12. *The marginal posterior distributions of Δ_{AB} (first panel), Δ_{AC} (second panel), and Δ_{AD} (third panel) with $L_{\text{prof}}(\Delta)$ superimposed. Vertical red dashed lines indicate blinded true time delays.*

TABLE 2

Estimates of Δ_{AB} , Δ_{AC} , and Δ_{AD} ; the profile likelihood estimates, $\hat{\Delta}_{\text{mean}}$ and $\hat{V}^{0.5}$ are given in the $E(\Delta|\mathbf{x}(\mathbf{t}), \mathbf{y}(\mathbf{t}))$ and $SD \equiv SD(\Delta|\mathbf{x}(\mathbf{t}), \mathbf{y}(\mathbf{t}))$ columns, where $\text{Error} \equiv |\Delta_{\text{true}} - E(\Delta|\mathbf{x}(\mathbf{t}), \mathbf{y}(\mathbf{t}))|$ with Δ_{true} indicating the true time delay, i.e., $\Delta_{AB} = 59.88$, $\Delta_{AC} = 23.87$ and $\Delta_{AD} = 51.14$, and $\chi \equiv \text{Error}/SD(\Delta|\mathbf{x}(\mathbf{t}), \mathbf{y}(\mathbf{t}))$.

	Method	$E(\Delta \mathbf{x}(\mathbf{t}), \mathbf{y}(\mathbf{t}))$	$\hat{\Delta}_{\text{MLE}}$	SD	Δ_{true}	Error	χ
Δ_{AB}	Bayesian	59.21		0.52	59.88	0.67	1.29
	Profile likelihood	59.21	59.38	0.51	59.88	0.67	1.31
Δ_{AC}	Bayesian	23.55		0.20	23.87	0.32	1.60
	Profile likelihood	23.54	23.58	0.19	23.87	0.33	1.74
Δ_{AD}	Bayesian	51.03		0.39	51.14	0.11	0.28
	Profile likelihood	51.03	51.08	0.38	51.14	0.11	0.29

are summarized in Table 2. The Bayesian estimates and profile likelihood approximations are quite similar and both produce estimates within two standard deviations of the truth (all $\chi \leq 1.74$).

5.3. *Quasar Q0957+561.* The first known gravitationally (doubly) lensed quasar *Q0957+561* was discovered by Walsh, Carswell and Weymann (1979) who suggested that a strong gravitational lensing may have formed the two images. Here we analyze the most recent observation of this quasar. This observation was made by the United States Naval Observatory in 2008–2011 (Hainline et al., 2012). The data were observed on 57 nights and are plotted in the first panel of Figure 13. The feasible range for Δ is $[-1178.939, 1178.939]$.

Inspection of $L_{\text{prof}}(\Delta)$ revealed one dominant mode. Using a uniform prior distribution of Δ over its range and $\sigma^2 \sim \text{IG}(1, 2/10^7)$, we ran three MCMC

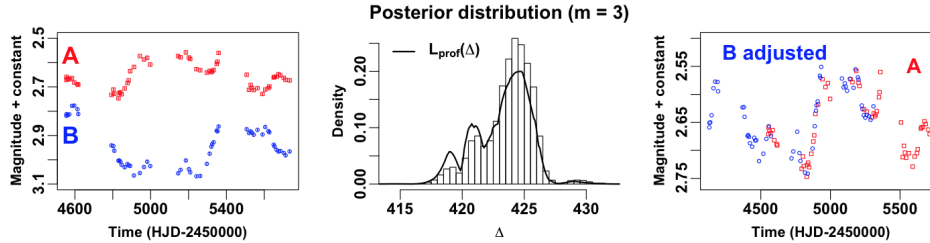


FIG 13. Observations of Quasar *Q0957+561* from Hainline et al. (2012) are plotted in the first panel. The second panel exhibits the marginal posterior distribution of Δ with $L_{\text{prof}}(\Delta)$ superimposed. We shift light curve B by $\hat{\Delta}_{\text{MLE}}$ (x -axis) and subtract the estimated third-order polynomial regression (obtained by the profile likelihood at $\hat{\Delta}_{\text{MLE}}$) in the third panel. HJD indicates the Heliocentric Julian date.

TABLE 3

Historical time delay estimates and standard errors (SE) for Q0957+561 (*r*-band). Our work provides the posterior mean and standard deviation of Δ and profile likelihood approximations to them. [Serra-Ricart et al. \(1999\)](#), [Oscoz et al. \(1997, 2001\)](#) and [Pelt et al. \(1996\)](#) used a bootstrapping method to calculate the SE.

Researchers	Method	Estimate	SE
Pelt et al. (1996)	Dispersion method	423	6
Oscoz et al. (1997)	Discrete cross-correlation & Dispersion	424	3
Serra-Ricart et al. (1999)	Least square optimization via auto-& cross-correlation	425	4
Oscoz et al. (2001)	Discrete correlation function (DCF)	426	5
	Discrete auto-& cross-correlation	423	2
	Z-transformed DCF	420	8
	χ^2 -minimization	422	3
This work	Bayesian	423.73	2.02
	Profile likelihood	423.21	2.81

chains near this mode; the GRD for Δ is 1.0001. The second panel of Figure 13 shows the marginal posterior distribution of Δ with $L_{\text{prof}}(\Delta)$ superimposed. It took 1,243 seconds to map $L_{\text{prof}}(\Delta)$ and 71 seconds on average for each MCMC chain.

In this case the dominant mode of Δ has more complex structure as detected by both $L_{\text{prof}}(\Delta)$ and the MCMC sample, see the second panel of Figure 13. In the third panel of Figure 13, we shift light curve B by $\hat{\Delta}_{\text{MLE}}$ (x -axis) and subtract the estimated third-order polynomial regression. The fitted microlensing model matches the intrinsic fluctuations of the two light curves.

Estimates based on different observations of Q0957+561 appear in Table 3. Although the observations span different time periods, the resulting estimates, including ours, are broadly consistent. Though the posterior mean and standard deviation may be difficult to interpret with a multimodal posterior distribution, we include them for comparison.

5.4. *Quasar J1029+2623*. [Inada et al. \(2006\)](#) discovered the gravitationally lensed quasar *J1029+2623* whose time delay is the second largest yet observed. Though *J1029+2623* has three images (A, B, and C), [Fohlmeister et al. \(2013\)](#) merged B and C because C is indistinguishable from B due to its faintness and proximity. They published its data (A, B+C) with 279 epochs monitored at the Fred Lawrence Whipple observatory from January 2007 to

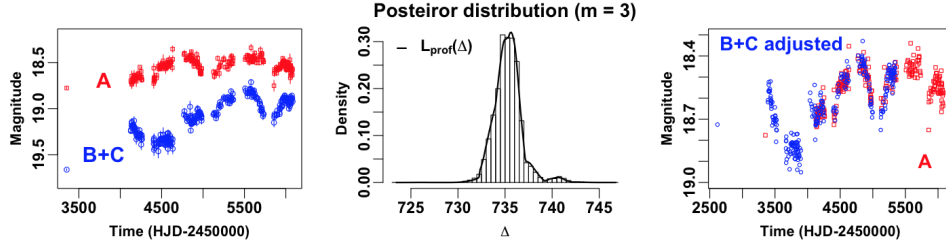


FIG 14. We plot the observations of Quasar *J1029+2623* from [Fohlmeister et al. \(2013\)](#) in the first panel. The second panel exhibits the marginal posterior distribution of Δ with $L_{\text{prof}}(\Delta)$ superimposed. We shift light curve *B + C* by $\hat{\Delta}_{MLE}$ (*x*-axis) and subtract the estimated third-order polynomial regression (obtained by the profile likelihood at $\hat{\Delta}_{MLE}$) in the last panel. *HJD* indicates the Heliocentric Julian date.

June 2012. The first panel in Figure 14 shows these data. The feasible range of Δ is $[-2729.759, 2729.759]$.

We confirmed a dominant mode via $L_{\text{prof}}(\Delta)$ and using a uniform prior distribution of Δ over its range and $\sigma^2 \sim \text{IG}(1, 2/10^7)$, we initiated three MCMC chains near this mode; the GRD for Δ is 1.0009. We display the marginal posterior distribution of Δ in the second panel of Figure 14 with $L_{\text{prof}}(\Delta)$ superimposed. It took 33,683 seconds to map $L_{\text{prof}}(\Delta)$ and 311 seconds on average for each MCMC chain. The posterior distribution and the profile likelihood are almost identical. In the third panel, we shift light curve *B* by $\hat{\Delta}_{MLE}$ (*x*-axis) and subtract the estimated third-order polynomial regression. Again, the fitted microlensing model finds a good match of the two light curves.

We compare our estimates in Table 4 with historical estimates that are based on the same data. The Bayesian method uses 5% and 95% quantiles of

TABLE 4

Historical time delay estimates and 90% confidence intervals for J1029+2623. Our work provides the posterior mean and 90% posterior interval of Δ and profile likelihood approximations to them. Fohlmeister et al. (2013) did not specify how they produced the sampling distribution of Δ . Kumar, Stalin and Prabhu (2014) used a parametric bootstrapping method.

Researchers	Method	Estimate	90% Interval
Fohlmeister et al. (2013)	χ^2 -minimization (AIC, BIC)	744	(734, 754)
Kumar, Stalin, and Prabhu (2014)	Difference-smoothing	743.5	(734.6, 752.4)
This work	Bayesian	735.31	(733.08, 737.71)
	Profile likelihood	733.11	(732.94, 738.44)

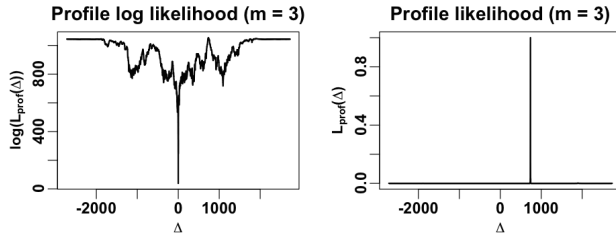


FIG 15. The profile log likelihood (left) and the profile likelihood (right) of Δ over its feasible range under the microlensing model ($m = 3$). Although the profile likelihood shows a dominant mode near 735 days, there are small modes near -2,000 and 1,800 days.

the posterior samples of Δ as the 90% posterior interval. To obtain the 90% interval estimate for Δ via the profile likelihood, we draw 50,000 samples of Δ using the empirical CDF of the (normalized) profile likelihood and choose their 5% and 95% quantiles.

The shape of the posterior distribution of Δ is almost identical to that of the profile likelihood in the second panel of Figure 14. However, the posterior mean of Δ is larger than the profile approximation, $\hat{\Delta}_{\text{mean}}$, by about two days. This is because there are two small modes near -2,000 and 1,800 days, see the second panel of Figure 15. Because the mode near 735 days overwhelmed the other modes, it is reasonable to focus on the mode near 735 days as the Bayesian result does. Overall, our point estimates are smaller than the historical estimates by about ten days, though our 90% posterior intervals overlap with the other historical 90% confidence intervals in Table 4.

6. Concluding remarks. Accurately estimating time delays among gravitationally lensed quasar images is a key to making fundamental measurements of the current expansion rate of the Universe and dark energy (Refsdal, 1964; Linder, 2011). The Large Synoptic Survey Telescope (LSST Science Collaboration, 2009) will produce extensive time series data on thousands of multiply lensed quasars starting in 2022. Anticipating this era of astronomical Big Data, we have improved the fully Bayesian model of Harva and Raychaudhury (2006) by leveraging recent advances in astrophysical and statistical modeling. We have added an Orstein-Uhlenbeck process to model the fluctuations in quasar light curves, a polynomial regression to account for microlensing, and a profile-likelihood-guided Bayesian strategy.

There are several opportunities to build upon our work in future research. It is desirable to implement more sophisticated methods of model selection such as information criteria to choose the complexity of the microlensing

trend. Though astrophysicists have used a cubic polynomial trend for microlensing models for some quasars so far, it would be better to have a fast and principled mechanism to determine the order given any data of gravitationally lensed quasars. Another avenue for further improvement is to constrain the range of the time delay by incorporating additional astrophysical information such as spatial positions of the images relative to the lensing galaxy, and an astrophysical model for the mass distribution of the lens. For quadruply-lensed quasar systems, constructing a Bayesian model to simultaneously analyze the four light curves, would allow us to coherently estimate the relative time delays without loss of information. Further improvements to the computational efficiency of our profile likelihood and MCMC strategies will enhance their effectiveness for analyzing the extensive time series datasets expected in the era of the LSST.

Acknowledgements. This work was conducted under the auspices of the CHASC International Astrostatistics Center. CHASC is supported by NSF grants DMS 1208791 and DMS 1209232. In addition, HT and XLM acknowledge support from the Harvard Statistics Department, KM is supported at Harvard by NSF grant AST-1211196, VLK and AS from a NASA contract to the Chandra X-Ray Center NAS8-03060, and DvD from a Wolfson Research Merit Award provided by the British Royal Society and from a Marie-Curie Career Integration Grant provided by the European Commission. In addition, we thank CHASC members for many helpful discussions.

SUPPLEMENTARY MATERIAL

Supplement: R codes and data

(; Rcode_data.zip). This zip file contains all the codes written in R (Rcode.R) and data (Data.zip) used in this article. An R package, `timedelay`, that implements the Bayesian and profile likelihood methods is publicly available at CRAN (<https://cran.r-project.org/package=timedelay>)

References.

- BERGER, J. O., LISEO, B., WOLPERT, R. L. et al. (1999). Integrated Likelihood Methods for Eliminating Nuisance Parameters. *Statistical Science* **14** 1–28.
- BERK, D. E. V., WILHITE, B. C., KRON, R. G., ANDERSON, S. F., BRUNNER, R. J., HALL, P. B., IVEZIĆ, Ž., RICHARDS, G. T., SCHNEIDER, D. P., YORK, D. G. et al. (2004). The Ensemble Photometric Variability of 25,000 Quasars in the Sloan Digital Sky Survey. *The Astrophysical Journal* **601** 692.
- BLANDFORD, R. and NARAYAN, R. (1992). Cosmological Applications of Gravitational Lensing. *Annual Review of Astronomy and Astrophysics* **30** 311–358.
- BROOKS, S., GELMAN, A., JONES, G. and MENG, X.-L. (2011). *Handbook of Markov Chain Monte Carlo*. CRC press.

- CHANG, K. and REFSDAL, S. (1979). Flux Variations of QSO 0957+ 561 A, B and Image Splitting by Stars Near the Light Path. *Nature* **282** 561–564.
- LSST SCIENCE COLLABORATION (2009). LSST science book, Version 2.0. *arXiv* **912**.
- DAVISON, A. C. (2003). *Statistical Models*. Cambridge University Press.
- DOBLER, G., FASSNACHT, C., TREU, T., MARSHALL, P. J., LIAO, K., HOJJATI, A., LINDER, E. and RUMBAUGH, N. (2015). Strong Lens Time Delay Challenge. I. Experimental Design. *The Astrophysical Journal* **799** 168.
- FASSNACHT, C., PEARSON, T., READHEAD, A., BROWNE, I., KOOPMANS, L., MYERS, S. and WILKINSON, P. (1999). A Determination of H_0 with the CLASS Gravitational Lens B1608+ 656. I. Time Delay Measurements with the VLA. *The Astrophysical Journal* **527** 498.
- FISCHER, P., BERNSTEIN, G., RHEE, G. and TYSON, J. A. (1997). The Mass Distribution of the Cluster Q0957+561 from Gravitational Lensing. *The Astronomical Journal* **113** 521.
- FOHLMEISTER, J., KOCHANEK, C. S., FALCO, E. E., WAMBSGANSS, J., OGURI, M. and DAI, X. (2013). A Two-year Time Delay for the Lensed Quasar SDSS J1029+ 2623. *The Astrophysical Journal* **764** 186.
- GELMAN, A. and RUBIN, D. B. (1992). Inference from Iterative Simulation Using Multiple Sequences. *Statistical Science* 457–472.
- GELMAN, A., CARLIN, J. B., STERN, H. S., DUNSON, D. B., VEHTARI, A. and RUBIN, D. B. (2013). *Bayesian Data Analysis*. CRC press.
- HAINLINE, L. J., MORGAN, C. W., BEACH, J. N., KOCHANEK, C., HARRIS, H. C., TILLEMANN, T., FADELY, R., FALCO, E. E. and LE, T. X. (2012). A New Microlensing Event in the Doubly Imaged Quasar Q 0957+ 561. *The Astrophysical Journal* **744** 104.
- HARVA, M. and RAYCHAUDHURY, S. (2006). *Bayesian Estimation of Time Delays Between Unevenly Sampled Signals*. IEEE.
- HOJJATI, A., KIM, A. G. and LINDER, E. V. (2013). Robust Strong Lensing Time Delay Estimation. *Physical Review D* **87** 123512.
- INADA, N., OGURI, M., MOROKUMA, T., DOI, M., YASUDA, N., BECKER, R. H., RICHARDS, G. T., KOCHANEK, C. S., KAYO, I., KONISHI, K. et al. (2006). SDSS J1029+ 2623: A Gravitationally Lensed Quasar with an Image Separation of 225. *The Astrophysical Journal Letters* **653** L97.
- KELLY, B. C., BECHTOLD, J. and SIEMIGINOWSKA, A. (2009). Are the Variations in Quasar Optical Flux Driven by Thermal Fluctuations? *The Astrophysical Journal* **698** 895.
- KOCHANEK, C., MORGAN, N., FALCO, E., MCLEOD, B., WINN, J., DEMBICKY, J. and KETZEBACK, B. (2006). The Time Delays of Gravitational Lens HE 0435–1223: An Early-Type Galaxy with a Rising Rotation Curve. *The Astrophysical Journal* **640** 47.
- KOZŁOWSKI, S. and KOCHANEK, C. S. (2009). Discovery of 5000 Active Galactic Nuclei Behind the Magellanic Clouds. *The Astrophysical Journal* **701** 508.
- KOZŁOWSKI, S., KOCHANEK, C. S., UDALSKI, A., SOSZYŃSKI, I., SZYMAŃSKI, M., KUBIAK, M., PIETRZYŃSKI, G., SZEWCZYK, O., ULACZYK, K., POLESKI, R. et al. (2010). Quantifying Quasar Variability as Part of a General Approach to Classifying Continuously Varying Sources. *The Astrophysical Journal* **708** 927.
- KUMAR, S. R., STALIN, C. and PRABHU, T. (2014). H_0 from 11 Well Measured Time-delay Lenses. *Astronomy and Astrophysics* **580**.
- LIAO, K., TREU, T., MARSHALL, P., FASSNACHT, C. D., RUMBAUGH, N., DOBLER, G., AGHAMOUSA, A., BONVIN, V., COURBIN, F., HOJJATI, A., JACKSON, N., KASHYAP, V., RATHNA KUMAR, S., LINDER, E., MANDEL, K., MENG, X. L., MEYLAN, G., MOUSTAKAS, L. A., PRABHU, T. P., ROMERO-WOLF, A., SHAFIELOO, A., SIEMIGI-

- NOWSKA, A., STALIN, C. S., TAK, H., TEWES, M. and VAN DYK, D. (2015). Strong Lens Time Delay Challenge: II. Results of TDC1. *The Astrophysical Journal* **800** 11.
- LINDER, E. V. (2011). Lensing Time Delays and Cosmological Complementarity. *Phys. Rev. D* **84** 123529.
- LIU, J. S. (2008). *Monte Carlo Strategies in Scientific Computing*. Springer Science & Business Media.
- MACLEOD, C., IVEZIĆ, Ž., KOCHANÉK, C., KOZŁOWSKI, S., KELLY, B., BULLOCK, E., KIMBALL, A., SESAR, B., WESTMAN, D., BROOKS, K. et al. (2010). Modeling the Time Variability of SDSS Stripe 82 Quasars as a Damped Random Walk. *The Astrophysical Journal* **721** 1014.
- MORGAN, C. W., HAINLINE, L. J., CHEN, B., TEWES, M., KOCHANÉK, C. S., DAI, X., KOZŁOWSKI, S., BLACKBURN, J. A., MOSQUERA, A. M., CHARTAS, G. et al. (2012). Further Evidence that Quasar X-ray Emitting Regions are Compact: X-ray and Optical Microlensing in the Lensed Quasar Q J0158-4325. *The Astrophysical Journal* **756** 52.
- MUNOZ, J., FALCO, E., KOCHANÉK, C., LEHÁR, J., MCLEOD, B., IMPEY, C., RIX, H.-W. and PENG, C. (1998). The CASTLES project. *Astrophysics and Space Science* **263** 51–54.
- OSCOZ, A., MEDIAVILLA, E., GOICOECHEA, L. J., SERRA-RICART, M. and BUITRAGO, J. (1997). Time Delay of QSO 0957+ 561 and Cosmological Implications. *The Astrophysical Journal Letters* **479** L89.
- OSCOZ, A., ALCALDE, D., SERRA-RICART, M., MEDIAVILLA, E., ABAJAS, C., BARRERA, R., LICANDRO, J., MOTTA, V. and MUNOZ, J. (2001). Time delay in QSO 0957+ 561 from 1984-1999 optical data. *The Astrophysical Journal* **552** 81.
- PELT, J., HOFF, W., KAYSER, R., REFSDAL, S. and SCHRAMM, T. (1994). Time Delay Controversy on QSO 0957+ 561 not yet Decided. *arXiv preprint astro-ph/9401013*.
- PELT, J., KAYSER, R., REFSDAL, S. and SCHRAMM, T. (1996). The Light Curve and the Time Delay of QSO 0957+ 561. *arXiv preprint astro-ph/9501036*.
- REFSDAL, S. (1964). The Gravitational Lens Effect. *Monthly Notices of the Royal Astronomical Society* **128** pp. 295-306.
- ROBERTS, G. O. and ROSENTHAL, J. S. (2007). Coupling and Ergodicity of Adaptive Markov Chain Monte Carlo Algorithms. *Journal of applied probability* 458–475.
- SCHNEIDER, P., EHLERS, J. and FALCO, E. (1992). *Gravitational Lenses*. Springer.
- SCHNEIDER, P., WAMBSGANSS, J. and KOCHANÉK, C. S. (2006). *Gravitational Lensing: Strong, Weak and Micro*. Springer.
- SERRA-RICART, M., OSCOZ, A., SANCHÍS, T., MEDIAVILLA, E., GOICOECHEA, L. J., LICANDRO, J., ALCALDE, D. and GIL-MERINO, R. (1999). BVRI Photometry of QSO 0957+ 561A, B: Observations, New Reduction Method, and Time Delay. *The Astrophysical Journal* **526** 40.
- SUYU, S., AUGER, M., HILBERT, S., MARSHALL, P., TEWES, M., TREU, T., FASSNACHT, C., KOOPMANS, L., SLUSE, D., BLANDFORD, R. et al. (2013). Two Accurate Time-delay Distances from Strong Lensing: Implications for Cosmology. *The Astrophysical Journal* **766** 70.
- TEWES, M., COURBIN, F. and MEYLAN, G. (2012). COSMOGRAIL: the COSmological MONitoring of GRAvItational Lenses XI. Techniques for time delay measurement in presence of microlensing. *arXiv preprint arXiv:1208.5598*.
- TIERNEY, L. (1994). Markov Chains for Exploring Posterior Distributions. *The Annals of Statistics* 1701–1728.
- UHLENBECK, G. E. and ORNSTEIN, L. S. (1930). On the Theory of the Brownian Motion. *Physical review* **36** 823.
- VAN DYK, D. A. and MENG, X.-L. (2001). The Art of Data Augmentation. *Journal of*

Computational and Graphical Statistics **10**.

WALSH, D., CARSWELL, R. and WEYMANN, R. (1979). 0957+ 561 A, B- Twin Quasistellar Objects or Gravitational Lens. *Nature* **279** 381–384.

YU, Y. and MENG, X.-L. (2011). To Center or not to Center: That is not the Question? An Ancillarity–Sufficiency Interweaving Strategy (ASIS) for Boosting MCMC Efficiency. *Journal of Computational and Graphical Statistics* **20** 531–570.

ZU, Y., KOCHANNEK, C., KOZŁOWSKI, S. and UDALSKI, A. (2013). Is Quasar Optical Variability a Damped Random Walk? *The Astrophysical Journal* **765** 106.

APPENDIX A: CONDITIONAL DISTRIBUTIONS OF $\mathbf{X}(\cdot)$

We define a combined light curve $z(\cdot)$ as follows. The observed magnitude at time t_j^Δ is denoted by $z(t_j^\Delta)$, which is either $x(t_j)$ or $y(t_j - \Delta) - \mathbf{w}_m^\top(t_j - \Delta)\boldsymbol{\beta}$ depending on whether t_j^Δ is one of \mathbf{t} or one of $\mathbf{t} - \Delta$. The observed measurement error is denoted by $\xi(t_j^\Delta)$, which is either $\delta(t_j)$ for $x(t_j)$ or $\eta(t_j)$ for $y(t_j - \Delta) - \mathbf{w}_m^\top(t_j - \Delta)\boldsymbol{\beta}$. We also define $z'(t_j^\Delta)$ as the centered observed magnitude at time t_j^Δ , which is either $x(t_j) - \mu$ or $y(t_j - \Delta) - \mathbf{w}_m^\top(t_j - \Delta)\boldsymbol{\beta} - \mu$ for $j = 1, 2, \dots, 2n$. We introduce the centered latent magnitudes $\mathbf{X}'(\mathbf{t}^\Delta) = \mathbf{X}(\mathbf{t}^\Delta) - \mu$ for notational simplicity. Also, let “ $< t_j^\Delta$ ” denote the set $\{t_i^\Delta : i = 1, 2, \dots, j - 1\}$ and “ $> t_j^\Delta$ ” denote $\{t_i^\Delta : i = j + 1, j + 2, \dots, 2n\}$. We sample $p(\mathbf{X}'(\mathbf{t}^\Delta) \mid \Delta, \boldsymbol{\beta}, \mu, \sigma^2, \tau, \mathbf{x}(\mathbf{t}), \mathbf{y}(\mathbf{t}))$ by sequentially sampling from its complete conditional distributions, and return $\mathbf{X}'(\mathbf{t}^\Delta)$ to the non-centered latent magnitudes, i.e., $\mathbf{X}(\mathbf{t}^\Delta) = \mathbf{X}'(\mathbf{t}^\Delta) + \mu$ at the end of sampling. To save space, we suppress conditioning on $\Delta, \boldsymbol{\beta}, \mu, \sigma^2, \tau, \mathbf{x}(\mathbf{t}), \mathbf{y}(\mathbf{t})$. The complete conditional distributions are given by

$$(A.1) \quad X'(t_1^\Delta) \mid \mathbf{X}'(> t_1^\Delta) \sim \text{N} \left[(1 - B_1^\Delta)z'(t_1^\Delta) + B_1^\Delta a_2 X'(t_2^\Delta), (1 - B_1^\Delta)\xi^2(t_1^\Delta) \right],$$

where $B_1^\Delta = \xi^2(t_1^\Delta) / [\xi^2(t_1^\Delta) + \tau\sigma^2(1 - a_2^2)/2]$. For $j = 2, 3, \dots, 2n - 1$,

$$(A.2) \quad X'(t_j^\Delta) \mid \mathbf{X}'(< t_j^\Delta), \mathbf{X}'(> t_j^\Delta) \\ \sim \text{N} \left[(1 - B_j^\Delta)z'(t_j^\Delta) + B_j^\Delta \left((1 - B_j) \frac{X'(t_{j+1}^\Delta)}{a_{j+1}} + B_j a_j X'(t_{j-1}^\Delta) \right), (1 - B_j^\Delta)\xi^2(t_j^\Delta) \right],$$

where $B_j^\Delta = \xi^2(t_j^\Delta) / \left[\xi^2(t_j^\Delta) + \frac{\tau\sigma^2}{2} \frac{(1 - a_j^2)(1 - a_{j+1}^2)}{1 - a_j^2 a_{j+1}^2} \right]$ and $B_j = \frac{1 - a_{j+1}^2}{1 - a_j^2 a_{j+1}^2}$. Lastly,

$$(A.3) \quad X'(t_{2n}^\Delta) \mid \mathbf{X}'(< t_{2n}^\Delta) \sim \text{N} \left[(1 - B_{2n}^\Delta)z'(t_{2n}^\Delta) + B_{2n}^\Delta a_{2n} X'(t_{2n-1}^\Delta), (1 - B_{2n}^\Delta)\xi^2(t_{2n}^\Delta) \right],$$

where $B_{2n}^\Delta = \xi^2(t_{2n}^\Delta) / [\xi^2(t_{2n}^\Delta) + \tau\sigma^2(1 - a_{2n}^2)/2]$ and $a_j = \exp(-(t_j^\Delta - t_{j-1}^\Delta)/\tau)$.

APPENDIX B: THE LIKELIHOOD FUNCTION OF PARAMETERS.

We use the same notation for the observed data as is defined in Appendix A, i.e., $z'(t_j^\Delta)$ and $\xi(t_j^\Delta)$. Let $D_j = \{z'(t_1^\Delta), z'(t_2^\Delta), \dots, z'(t_j^\Delta)\}$. For

$j = 1, 2, \dots, 2n$, the posterior predictive density functions of $z'(t_j^\Delta)$ with $\mathbf{X}(\mathbf{t}^\Delta)$ integrated out are

$$(B.1) \quad z'(t_1^\Delta) \sim N[0, \xi(t_1^\Delta)^2 + \tau\sigma^2/2],$$

$$(B.2) \quad z'(t_j^\Delta) | D_{j-1} \sim N[a_j\mu_{j-1}, \xi(t_j^\Delta)^2 + a_j^2\Omega_{j-1} + \tau\sigma^2(1 - a_j^2)/2],$$

where $\mu_1 = (1 - B_1)z'(t_1^\Delta)$, $\mu_j = (1 - B_j)z'(t_j^\Delta) + B_j a_j \mu_{j-1}$, $\Omega_j = (1 - B_j)\xi(t_j^\Delta)^2$, $B_1 = \xi(t_1^\Delta)^2 / [\xi(t_1^\Delta)^2 + \tau\sigma^2/2]$, $B_j = \xi(t_j^\Delta)^2 / [\xi(t_j^\Delta)^2 + a_j^2\Omega_{j-1} + \tau\sigma^2(1 - a_j^2)/2]$. The likelihood function of $(\Delta, \boldsymbol{\beta}, \mu, \sigma^2, \tau)$ is the product of the Gaussian densities as follows.

$$(B.3) \quad L(\Delta, \boldsymbol{\beta}, \mu, \sigma^2, \tau) \propto p(z'(t_1^\Delta)) \times \prod_{j=2}^{2n} p(z'(t_j^\Delta) | D_{j-1}).$$

Given the values of $(\boldsymbol{\beta}, \mu, \sigma^2, \tau)$, $L(\Delta, \boldsymbol{\beta}, \mu, \sigma^2, \tau)$ is proportional to the marginalized conditional posterior density $p(\Delta | \boldsymbol{\beta}, \mu, \sigma^2, \tau, \mathbf{x}(\mathbf{t}), \mathbf{y}(\mathbf{t}))$ for $\Delta \in [u_1, u_2]$ and is zero elsewhere.

APPENDIX C: METROPOLIS-HASTINGS WITHIN GIBBS SAMPLER

We specify the steps of the DA MHwG sampler, (3.2)-(3.5), with $\mathbf{x}(\mathbf{t})$ and $\mathbf{y}(\mathbf{t})$ suppressed in the condition. We sample $\boldsymbol{\beta}$ from its Gaussian conditional posterior distribution as follows. With a n by n diagonal matrix V whose diagonal elements are $\boldsymbol{\eta}^2(\mathbf{t})$,

$$(C.1) \quad \boldsymbol{\beta} | \mu, \sigma, \tau, \mathbf{X}(\mathbf{t}^\Delta), \Delta \sim N_{m+1} \left[J^{-1} \mathbf{W}_m(\mathbf{t} - \Delta)^\top V^{-1} \mathbf{u}, J^{-1} \right],$$

where $J \equiv \mathbf{W}_m^\top(\mathbf{t} - \Delta) V^{-1} \mathbf{W}_m(\mathbf{t} - \Delta) + 10^{-5} I_{m+1}$ and $\mathbf{u} \equiv \mathbf{y}(\mathbf{t}) - \mathbf{X}(\mathbf{t} - \Delta)$.

We sample μ from a truncated Gaussian conditional posterior distribution whose support is $[-30, 30]$; with $a_j = \exp(-(t_j^\Delta - t_{j-1}^\Delta)/\tau)$,

$$(C.2) \quad \mu | \sigma^2, \tau, \mathbf{X}(\mathbf{t}^\Delta), \Delta, \boldsymbol{\beta} \sim N \left[\frac{X(t_1^\Delta) + \sum_{j=2}^{2n} \frac{X(t_j^\Delta) - a_j X(t_{j-1}^\Delta)}{1 + a_j}}{1 + \sum_{j=2}^{2n} \frac{1 - a_j}{1 + a_j}}, \frac{\tau\sigma^2/2}{1 + \sum_{j=2}^{2n} \frac{1 - a_j}{1 + a_j}} \right].$$

The parameter σ^2 has an inverse-Gamma conditional posterior distribution; with its prior distribution $p(\sigma^2) \propto \exp(-b_\sigma/\sigma^2)/(\sigma^2)^2 \cdot I_{\{\sigma^2 > 0\}}$,

$$(C.3) \quad \sigma^2 | \mu, \tau, \mathbf{X}(\mathbf{t}^\Delta), \Delta, \boldsymbol{\beta} \sim$$

$$\text{IG} \left(n + 1, b_\sigma + \frac{(X(t_1^\Delta) - \mu)^2}{\tau} + \sum_{j=2}^{2n} \frac{[(X(t_j^\Delta) - \mu) - a_j(X(t_{j-1}^\Delta) - \mu)]^2}{\tau(1 - a_j^2)} \right).$$

The conditional posterior density function of τ is known up to a normalizing constant; with its prior distribution $p(\tau) \propto \exp(-1/\tau)/\tau^2 \cdot I_{\{\tau>0\}}$,

$$(C.4) \quad p(\tau \mid \mu, \sigma^2, \mathbf{X}(\mathbf{t}^\Delta), \Delta, \boldsymbol{\beta}) \propto \frac{\exp \left(-\frac{1}{\tau} - \frac{(X(t_1^\Delta) - \mu)^2}{\tau\sigma^2} - \sum_{j=2}^{2n} \frac{[(X(t_j^\Delta) - \mu) - a_j(X(t_{j-1}^\Delta) - \mu)]^2}{\tau\sigma^2(1 - a_j^2)} \right)}{\tau^{n+2} \cdot \prod_{j=2}^{2n} (1 - a_j^2)^{1/2}} \cdot I_{\{\tau>0\}}.$$

To sample τ from (C.4), we use a M-H step with a Gaussian proposal density $N[\log(\tau), \phi^2]$ on a logarithmic scale where ϕ is a proposal scale tuned to produce reasonable acceptance rate.

To implement the ASIS, we need a conditional posterior distribution for $\boldsymbol{\beta}$ given $\mathbf{K}(\mathbf{t}^\Delta)$ used in (3.14). Let $K'(t^\Delta) \equiv K(t^\Delta) - \mu$, B be a $2n$ by $(m+1)$ matrix whose j th row is $(\mathbf{w}_m(t_j^\Delta) - a_j \times \mathbf{w}_m(t_{j-1}^\Delta))^\top$, L be a $2n$ by $2n$ diagonal matrix whose j th diagonal element is $\tau\sigma^2(1 - a_j^2)/2$, \mathbf{b} be a $2n$ by 1 vector whose j th element is $K'(t_j^\Delta) - a_j K'(t_{j-1}^\Delta)$, and finally $A \equiv B^\top L^{-1} B + 10^{-5} I_{(m+1)}$. Then,

$$(C.5) \quad \boldsymbol{\beta} \mid \mu, \sigma^2, \tau, K'(t^\Delta), \Delta, \mathbf{x}(\mathbf{t}), \mathbf{y}(\mathbf{t}) \sim N_{m+1} \left[A^{-1} B^\top L^{-1} \mathbf{b}, A^{-1} \right].$$

APPENDIX D: PROFILE LIKELIHOOD APPROXIMATELY PROPORTIONAL TO THE MARGINAL POSTERIOR

We show that $L_{\text{prof}}(\Delta)$ is approximately proportional to $p(\Delta \mid \mathbf{x}(\mathbf{t}), \mathbf{y}(\mathbf{t}))$. Let $\boldsymbol{\nu} \equiv (\boldsymbol{\beta}^\top, \boldsymbol{\theta}^\top)^\top$. Then,

$$(D.1) \quad p(\Delta \mid \mathbf{x}(\mathbf{t}), \mathbf{y}(\mathbf{t})) = \int L(\Delta, \boldsymbol{\nu}) p(\Delta, \boldsymbol{\nu}) d\boldsymbol{\nu} = k \int L(\Delta, \boldsymbol{\nu}) p(\boldsymbol{\nu} \mid \Delta) d\boldsymbol{\nu},$$

where k is a normalizing constant of the uniform prior distribution for Δ . We put a Jeffreys' prior on $\boldsymbol{\nu}$ given Δ , i.e., $p(\boldsymbol{\nu} \mid \Delta) \propto |I_\Delta(\boldsymbol{\nu})|^{0.5} d\boldsymbol{\nu}$, where $I_\Delta(\boldsymbol{\nu})$ is Fisher information defined as $-E [\partial^2 \log(L(\Delta, \boldsymbol{\nu})) / \partial \boldsymbol{\nu} \boldsymbol{\nu}^\top]$. The resulting $p(\Delta \mid \mathbf{x}(\mathbf{t}), \mathbf{y}(\mathbf{t}))$ is a Jeffreys-integrated marginal likelihood with its uniform prior (Berger et al., 1999). If we can approximate $l(\Delta, \boldsymbol{\nu}) \equiv \log(L(\Delta, \boldsymbol{\nu}))$ with respect to $\boldsymbol{\nu}$ by a second-order Taylor's series, e.g., under standard asymptotic arguments, then

$$(D.2) \quad l(\Delta, \boldsymbol{\nu}) \approx l(\Delta, \hat{\boldsymbol{\nu}}_\Delta) - (\boldsymbol{\nu} - \hat{\boldsymbol{\nu}}_\Delta)^\top [-l''(\Delta, \hat{\boldsymbol{\nu}}_\Delta)] (\boldsymbol{\nu} - \hat{\boldsymbol{\nu}}_\Delta) / 2,$$

where $\hat{\boldsymbol{\nu}}_\Delta = \arg \max_{\boldsymbol{\nu}} l(\Delta, \boldsymbol{\nu})$, and $l''(\Delta, \hat{\boldsymbol{\nu}}_\Delta) \equiv \partial^2 l(\Delta, \boldsymbol{\nu}) / \partial \boldsymbol{\nu} \boldsymbol{\nu}^\top |_{\boldsymbol{\nu}=\hat{\boldsymbol{\nu}}_\Delta}$, which results in

$$(D.3) \quad L(\Delta, \boldsymbol{\nu}) \approx \exp \left(l(\Delta, \hat{\boldsymbol{\nu}}_\Delta) - (\boldsymbol{\nu} - \hat{\boldsymbol{\nu}}_\Delta)^\top [-l''(\Delta, \hat{\boldsymbol{\nu}}_\Delta)] (\boldsymbol{\nu} - \hat{\boldsymbol{\nu}}_\Delta) / 2 \right).$$

Using this, we approximate the marginal posterior density function of Δ by

$$(D.4) \quad \begin{aligned} p(\Delta | \mathbf{x}(\mathbf{t}), \mathbf{y}(\mathbf{t})) &\approx k \times L(\Delta, \hat{\boldsymbol{\nu}}_\Delta) \\ &\times \int \exp \left(- (\boldsymbol{\nu} - \hat{\boldsymbol{\nu}}_\Delta)^\top [-l''(\Delta, \hat{\boldsymbol{\nu}}_\Delta)] (\boldsymbol{\nu} - \hat{\boldsymbol{\nu}}_\Delta) / 2 \right) |I_\Delta(\boldsymbol{\nu})|^{0.5} d\boldsymbol{\nu}. \end{aligned}$$

If we replace the Fisher information in (D.4), i.e., $I_\Delta(\boldsymbol{\nu})$, with the observed information, $-l''_\Delta(\hat{\boldsymbol{\nu}}_\Delta)$, under standard asymptotic arguments, then the integral in (D.4) leads to $(2\pi)^2$ because the integrand becomes a multivariate Gaussian density up to $(2\pi)^{-2}$. Finally,

$$(D.5) \quad p(\Delta | \mathbf{x}(\mathbf{t}), \mathbf{y}(\mathbf{t})) \approx k \times (2\pi)^2 \times L(\Delta, \hat{\boldsymbol{\nu}}_\Delta) = k \times (2\pi)^2 \times L_{\text{prof}}(\Delta) \propto L_{\text{prof}}(\Delta).$$

APPENDIX E: SENSITIVITY ANALYSES

To see the influence of prior distributions of τ and σ^2 on the posterior distribution of Δ , we conduct sensitivity analyses, varying the scale and shape parameters of their inverse-Gamma (IG) prior distributions.

As an example, we generate 80 observations based on $(\Delta, \beta_0, \mu, \sigma^2, \tau) = (50, 2, 0, 0.03^2, 100)$. The median observation cadence is 3 days and the measurement errors have a constant standard deviation of 0.005 magnitude.

When it comes to fitting the Bayesian model, we assume for simplicity that $\Delta \sim \text{Unif}[0, 100]$ a priori. We run three Markov chains, each of which has 10,000 iterations after 10,000 burn-ins. The initial values of Δ for the three chains are 20, 50, and 80, and those of (μ, σ, τ) are (0, 0.01, 200) the same for every chain. The initial value of β_0 is the average of $\mathbf{y}(\mathbf{t})$ minus that of $\mathbf{x}(\mathbf{t})$. The initial proposal scales, ψ and ϕ , are 10 and 3 days, respectively.

E.1. Sensitivity analysis of the prior distribution of τ . We look into the sensitivity of the posterior distribution of Δ to the shape parameter of the IG prior distribution of τ . We denote the shape parameter by a_τ and fix the scale parameter at 1. A reasonably small value of the scale parameter does not make any differences in the resultant posterior distribution of τ , not to mention that of Δ , because the conditional posterior density of τ in Appendix C.4 has exponential functions of τ in the exponent, which

dominates the scale parameter. We fix the $IG(1, b_\sigma)$ prior distribution for σ^2 , where $b_\sigma = 8 \times 10^{-6}$ mag² per day as explained in Appendix E.2.

Figure 16 shows the result of sensitivity analysis varying a_τ , the half of the degree of freedom in the corresponding inverse- χ^2 distribution; 0.1, 1, 10, 40, and 80 from the first column. Each column shows the posterior distribution of Δ (first row), that of $\log(\tau)$ (second row), and a scatter plot of posterior samples of $\log(\sigma)$ over those of $\log(\tau)$ (third row) obtained under each shape parameter. The dashed red lines indicate the generative true values.

The first four posterior distributions of Δ catch the generative value of Δ near the mode. However, when we assume too much information in the prior distribution by setting a_τ to 80 ($= n$), the posterior distribution of Δ in the last column becomes flat. A large a_τ concentrates the prior density on O-U processes with mean-reversion timescales τ much shorter than the observational cadence. A large value of a_τ moves the prior mode, $1/(1 + a_\tau)$, close to zero and a large degree of freedom ($2 * a_\tau$) for the prior distribution strongly influences the posterior of τ . Hence, the underlying light curves $\mathbf{X}(t^\Delta)$ governed by these O-U processes with small τ will effectively appear as white noise time series. The model will then be ineffective at constraining the time delay because this requires matching serially correlated fluctuation patterns in the light curves. The second row in Figure 16 shows that as a_τ

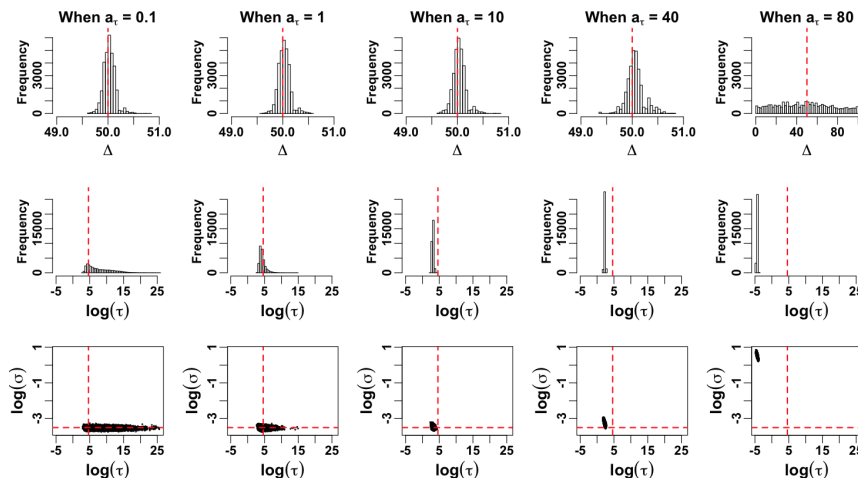


FIG 16. Each column shows posterior distribution of Δ (first row), that of $\log(\tau)$ (second row), and a scatter plot of $\log(\sigma)$ over $\log(\tau)$ (third row) obtained under a certain a_τ equal to 0.1, 1, 10, 40, and 80 from the first column. The true values of $(\Delta, \log(\sigma), \log(\tau))$ are $(50, -3.5, 4.6)$ represented by the dashed red lines on each plot. The posterior distribution of the time delay is robust to the shape parameter (a_τ) as long as it is reasonably small.

increases, the mode of the posterior distribution of $\log(\tau)$ gets smaller with a shorter right tail, getting farther away from the generative true value of $\log(\tau) = 4.6$. When the mode of $\log(\tau)$ reaches -5 ($\tau = \exp(-5) = 0.007 \ll 3$ -day observation cadence), the posterior distributions of Δ becomes flat.

E.2. Sensitivity analysis of the prior distribution of σ^2 . We check the sensitivity of the posterior distribution of Δ to the scale parameter b_σ of the $\text{IG}(1, b_\sigma)$ prior distribution of σ^2 . The effect of the unit shape parameter is negligible because the resultant shape parameter of the IG conditional posterior distribution of σ^2 in (C.3) is $n + 1$ in which n plays a dominant role in controlling the right tail behavior. We fix the $\text{IG}(1, 1)$ prior distribution for τ as explained in the previous section.

We display the result of the sensitivity analysis in Figure 17, where the values of b_σ are increasing from 0.001 to 10 from the first column. As the soft lower bound ($= b_\sigma/2$) increases from the left, the posterior distribution of the time delay becomes flatter. This is because the true value of σ^2 ($= 0.03^2$) is less than the soft lower bound. For example, when $b_\sigma = 10$ in the last column, the $\text{IG}(1, 10)$ prior distribution of σ^2 exponentially cuts off the probability density in the region to left of the mode, 5 mag² per day, which includes the true value of σ^2 ($= 0.03^2$). Because the true σ^2 is much smaller than

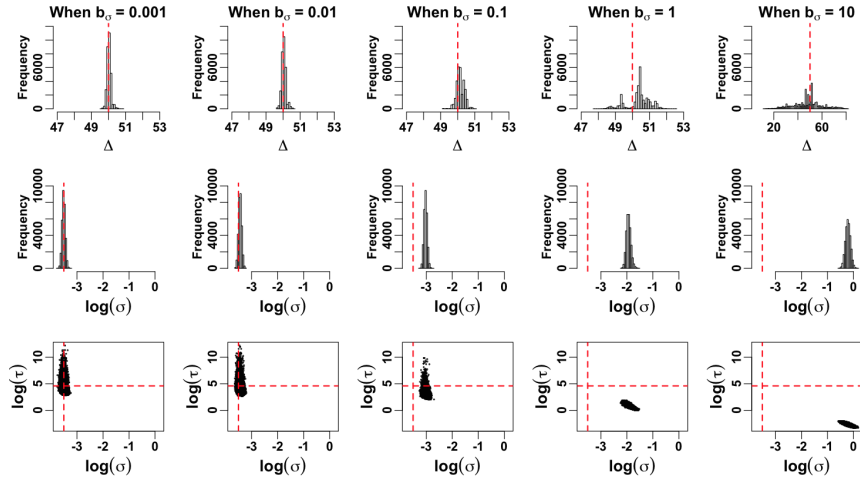


FIG 17. Each column shows posterior distribution of Δ (first row), that of $\log(\sigma)$ (second row), and a scatter plot of $\log(\tau)$ over $\log(\sigma)$ (third row) obtained under a certain scale parameter b_σ equal to 0.001, 0.01, 0.1, 1, and 10 from the first column. The true values of $(\Delta, \log(\sigma), \log(\tau))$ are $(50, -3.5, 4.6)$ represented by the dashed red lines on each plot. The posterior distributions of parameters recover the true values as the scale parameter (soft lower bound) decreases.

the soft lower bound, it is hard for the posterior distribution of σ^2 to move towards the true σ^2 by overcoming the exponential cut-off as the sample size is small. Also, due to the negative correlation between the posterior samples of τ and σ^2 as shown in the scatter plots, the larger the posterior sample of σ^2 is, the smaller the posterior sample of τ is. As the posterior samples of τ become smaller than the observational cadence, the posterior latent light curve $\mathbf{X}(t^\Delta)$ effectively becomes a white noise sequence. In this case, it is difficult to constrain the time delay.

The second row of Figure 17 shows that as the soft lower bound decreases from the right, the posterior distribution of $\log(\sigma)$ moves towards the true value of $\log(\sigma) = -3.5$ and starts containing it near the mode from the second column ($b_\sigma = 0.01$). The posterior distributions obtained under a value of b_σ smaller than 0.001 do not make noticeable differences, though not shown here. The small soft lower bound also helps the posterior samples of the other parameters cover their true values near the modes. For reference, although it may depend on data, the results became insensitive to the scale b_σ as the number of observations was more than 400.

HYUNGSUK TAK
DEPARTMENT OF STATISTICS
HARVARD UNIVERSITY
1 OXFORD STREET
CAMBRIDGE, MA, USA, 02138
E-MAIL: hyungsuk.tak@gmail.com

KAISEY MANDEL
HARVARD-SMITHSONIAN CENTER FOR ASTROPHYSICS
HARVARD UNIVERSITY
60 GARDEN STREET
CAMBRIDGE, MA, USA 02138
E-MAIL: kmandel@cfa.harvard.edu

DAVID A. VAN DYK
STATISTICS SECTION
DEPARTMENT OF MATHEMATICS
IMPERIAL COLLEGE LONDON
LONDON SW7 2AZ UK
E-MAIL: d.van-dyk@imperial.ac.uk

VINAY L. KASHYAP
HARVARD-SMITHSONIAN CENTER FOR ASTROPHYSICS
HARVARD UNIVERSITY
60 GARDEN STREET
CAMBRIDGE, MA, USA 02138
E-MAIL: vkashyap@cfa.harvard.edu

XIAO-LI MENG
DEPARTMENT OF STATISTICS
HARVARD UNIVERSITY
1 OXFORD STREET
CAMBRIDGE, MA, USA, 02138
E-MAIL: meng@fas.harvard.edu

ANETA SIEMIGINOWSKA
HARVARD-SMITHSONIAN CENTER FOR ASTROPHYSICS
HARVARD UNIVERSITY
60 GARDEN STREET
CAMBRIDGE, MA, USA 02138
E-MAIL: asiemiginowska@cfa.harvard.edu